A THESIS

FOR THE DEGREE OF DOCTOR OF PHILOSOPHY

Synthesis of Graphene Nanostructures and Nanocomposites for Memristive Devices

Junaid Ali

Department of Mechatronics Engineering

GRADUATE SCHOOL

JEJU NATIONAL UNIVERSITY

2016. 02

Synthesis of Graphene Nanostructures and Nanocomposites for Memristive Devices

Junaid Ali

(Supervised by Professor Kyung Hyun Choi)

A thesis submitted in partial fulfillment of the requirement for the degree of Doctor of Philosophy

2016. 02

The thesis has been examined and approved.

Thesis Director, Kyung-Hyun Choi, Professor, Department of Mechatronics Engineering

Yang-Hoi Doh, Professor, Department of Electronic Engineering

Jong-Hwan Lim, Professor, Department of Mechatronics Engineering

Kwang-Young Kim, Ph.D., Korea Institute of Machinery & Materials

Ki Rin Kwon, Professor, Department of Mechanical Engineering

Date

Department of Mechatronics Engineering

GRADUATE SCHOOL

JEJU NATIONAL UNIVERSITY

REPUBLIC OF KOREA

Dedicated to

My Parents, Family and Friends

&

Pakistan

ACKNOWLEDGEMENTS

In the Name of Allah, the Most Gracious, the Most Merciful. I would like to extend my humble gratitude to Allah Almighty, for bountiful blessings and gifts besides guidance and hope in hour of despair, courage and ability to make this sacred journey for learning and highest accolade of knowledge. I would pray that He grants me with ability to be a torch bearer for guiding and helping humanity.

This dissertation became a reality only because of Prof Choi, Kyung Hyun who as my supervisor and mentor guided, encouraged and challenged me throughout my postgraduate studies. Prof. Choi as a remarkable researcher and team manager provided me the research environment and vision to efficiently carry out my research. His stimulating seminars, brainstorming discussions and a never-ending appetite for brilliance I will admire and cherish forever. He has taken care of the research group as a family in matters related to family and finance besides studies and research.

I am extremely grateful to Dr. Waqar and Dr Nauman Malik who introduced me to my supervisor for postgraduate studies especially Dr Nauman who was instrumental in guiding me to start my higher studies in Jeju.

I have been fortunate enough to have had the support of so many people in the research group without them this thesis would have not been possible, Dr Zubair, Dr Adnan, Dr Naeem, Dr Maria, Dr Navaneethan, Dr Murtuza, Kamran, Ghayas. Shahid, Memoon, Muqeet, Jahanzeb, Srikanth, Jeong-beom, Bong Soo, Dang Hyun Woo, Yang Jin, SooWon, Jae hee, Hyeon Beom, and Go Bum are few names whose support was always there for me. I am also thankful to the wonderful friends, Dr Jake, Rashid, Farrukh, Dr Anil and others who shared my high and lows of postgraduate studies as well as provided the amicable environment during my stay at Jeju.

I am forever indebted to my mother who has been extremely understanding and supportive of my studies, and source of inspiration throughout my life. My current studies could have not been possible without the mentors, uncle Iftikhar, Prof Arshad Bhatti and Dr Ahmer Naweed. I would like to pay my heartiest gratitude to my wife Talat Ambreen who not only supported me throughout my postgraduate studies but also shared the responsibilities for taking care of my lovely daughter Hania when I was busy in my research. Without her support my accomplishment would have been undermined. I feel sorry for my daughter who was neglected during the course of my studies. I hope I will make up for the time they spent without me in future. I would also like to thank my

brothers Umair, Ubaid and Mudassar, my sisters, my in-laws Nasir, Shuaib and Nadeem, and my extended family who encouraged me throughout my studies and provided me the necessary moral support.

At the end I would honor the lovable and respectful Korean people for bearing with me despite language barrier. I thank the wonderful Korean nation, they deserve more than mentioned here.

Junaid Ali

Abbreviations and Notations

Density of states	DOS
Electrohydrodynamic atomization	EHDA
Electrohydrodynamic printing	EHD
Zero dimensional	0D
One dimensional	1D
Two Dimensional	2D
Graphene oxide	GO
Chemical vapor deposition	CVD
Reduced graphene oxide	rGO
Field-effect transistors	FETs
Carbon nanotube	CNT
X-ray diffration	XRD
Scanning electron microscopy	SEM
Photoluminescence	PL
N-methyl-pyrrolidone	NMP
1, 2-dichlorobenzene	DCB
Propylene glycol methyl ether acetate	PGMEA
Poly (4-vinyl phenol)	PVP
Selected area electron diffraction	SAED
Part per billion	ppb
Ultraviolet	UV
Resistive switching	RS
Compliance current	CC
High resistance state	HRS
Conducting filament	CF
Low resistance state	LRS
Transition metal dichalcogenides	TMDs
Metal atoms (M) and chalcogen atoms (X)	MX_2
Infrared	IR
High resolution transmission electron microscopy	HRTEM

Langmuir–Blodgett	LB
Silicon nanowire	SiNW
Nanostructured materials	NSMs

LIST OF FIGURES

LIST OF TABLES

Table of Contents

ABSTRACT

Graphene has had its share of fame and promise for fair part of our technological wonder and has kept churning out technological breakthroughs one after the other in past decade. The industry and academia are focused to discover and harness all the possible revelations this wonderful allotrope of carbon has on offer. Graphene and other members of 2D material family have been researched for wide range of properties such as photonic, electronic and mechanical properties. Resistive switching in materials has been studied in one way or the other since 1960s. However memristive devices have gained a lot of interest after experimental fabrication of the memristive device by Hewlett-Packard labs proving the mathematical proposition by Chua. This work is focused on synthesis of graphene nanostructures in form of nanoflakes and quantum dots, and the composites with polymers. The electrohydrodynamic atomization and other printed technologies were employed to fabricate resistive switching devices on PET and glass as substrate materials. The futuristic flexible printed memristors have also been explored and reported in this work. The technique employed to synthesize graphene quantum dots was used for synthesis of luminescent quantum dots of MoS_2 as well. Thus providing a promising technique worth further exploration for synthesis of quantum dots of other 2D materials.

Chapter 1. INTRODUCTION

Ever since the discovery of low dimensional carbon nanomaterials, fullerene (0D) and single walled carbon nanotube (CNT) (1D) several researchers attempted to isolate 2D graphitic material. The efforts paid off in 2004, in form of breakthrough in isolation and fabrication of graphene based transistor[1]. Graphene has since become a shining star on the horizon of materials science and condensed-matter physics. The fame and zeal for exploration undertaken for graphene has been unmatched for any material in history. It has exceptionally high crystal and electronic quality, and has already empowered new physics and potential applications, despite a very short time since its discovery by Geim and Novoselov[2] in 2004 while studying thin carbon films. Contradicting to the 70 years old argument by Landau and Peierls[3,4] that strictly two dimensional (2D) crystals were thermodynamically unstable and could not exist, graphene is here with proven proof for significance in terms of fundamental physics.

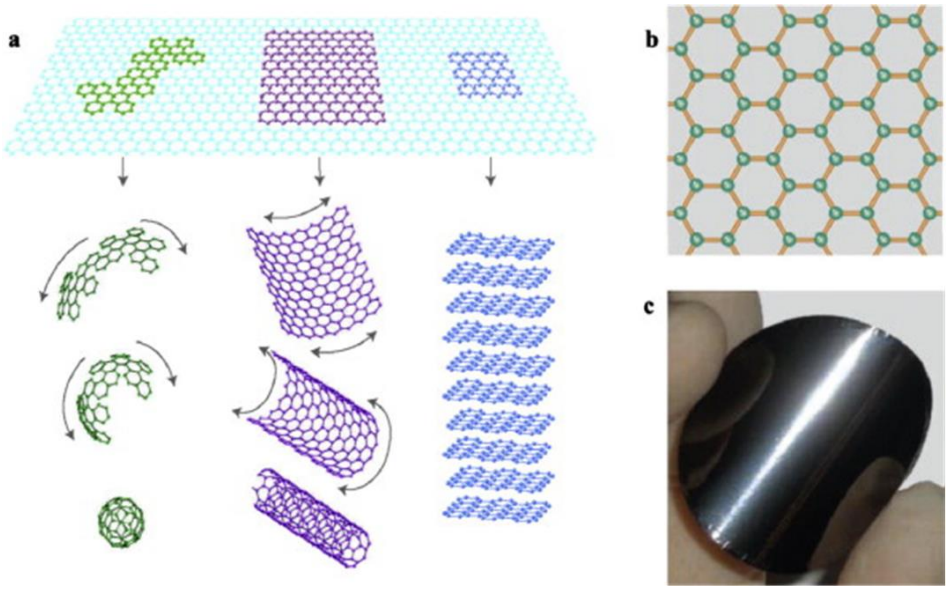

Figure 1-1: A C_{60} fullerene molecule, a carbon nanotube and graphite are in the order from left to right. Graphene, a single sheet of graphite, can be considered as building block of all these carbon structure (image produced from [5]. (b) Honey-comb lattice structure. (c) Dark shiny appearance of graphene. b and c images produced from [6].

Graphene discovery has conceptually set in motion research in a new class of materials only single-atom thick, paving way for low-dimensional nano material research towards both fundamental

physics and potential applications in all walks of life. Graphene sheets when rolled become carbon nanotubes, and repacking a graphene sheet constitutes C_{60} as shown in Figure 1-1(a).

1.1 Low Dimensional Materials

There are many layered materials having bonded strongly in-plane and a weak inter-layer bonding. This weak interlayer bonding has been a seed of opportunity for scientist to harvest. This single layer of atoms is called 2D material. The nanostructured materials (NSMs) of same material can give different properties, thus stirred up interest in synthesis of materials of different dimensions and shapes. By definition NSMs are solid materials with at least one dimension in nanometers. A nanocrystal smaller than the exciton Bohr radius for that material, in at least one dimension, is said to be quantum confined[7]. A zero dimensional (0D) material has its excited electrons confined in all three dimensions, thus behaving as a quasi-atom with discrete energy states. The carbon nanotubes, silicon nanowires, ZnO nanorods, nanobelts and nanoribbons are examples of 1D materials with confinement in two dimensions. The density of states for 2D materials, exhibits a quasi-continuous step-like increase with increasing excitation energy. Currently, fabrication of 2D materials has gained significant attention because of the physicochemical characteristics that are unique when compared to bulk counterpart. These 2D materials have shown promise for successful application in nano electronic devices[8–13].

Currently, 2D materials family has come a long way from graphene being the sole member. The family now includes transition metal dichalcogenides (TMDs), and layered metal oxides. The chemical formula MX_2, often trivially denotes the family with M a transition metal (Mo, Re, Nb, W, Ni or V) and X is a chalcogen (any of Se, Te, or S)[14–17].

1.2 Graphene

Graphene is the crystalline two-dimensional (2D) single atom thick sheet of carbon atoms arranged in a hexagonal lattice[2] as shown in Figure 1-1b). Graphene is transparent compared to dark charcoal black coloured graphite The simple yet effective work by Novoselov *et al.* [2] on electric field effect in graphene films was the first report on a stable isolated planar graphene. Figure 1-2 shows the patent trend for graphene from 2004 till the end of 2013[18], thus emphasizing the ever growing interest in graphene in both industry and academia. It has been a revolutionary material due to its unique thermal [19], optoelectronic [20], magnetic [21], superconducting [22] and

semiconducting properties.

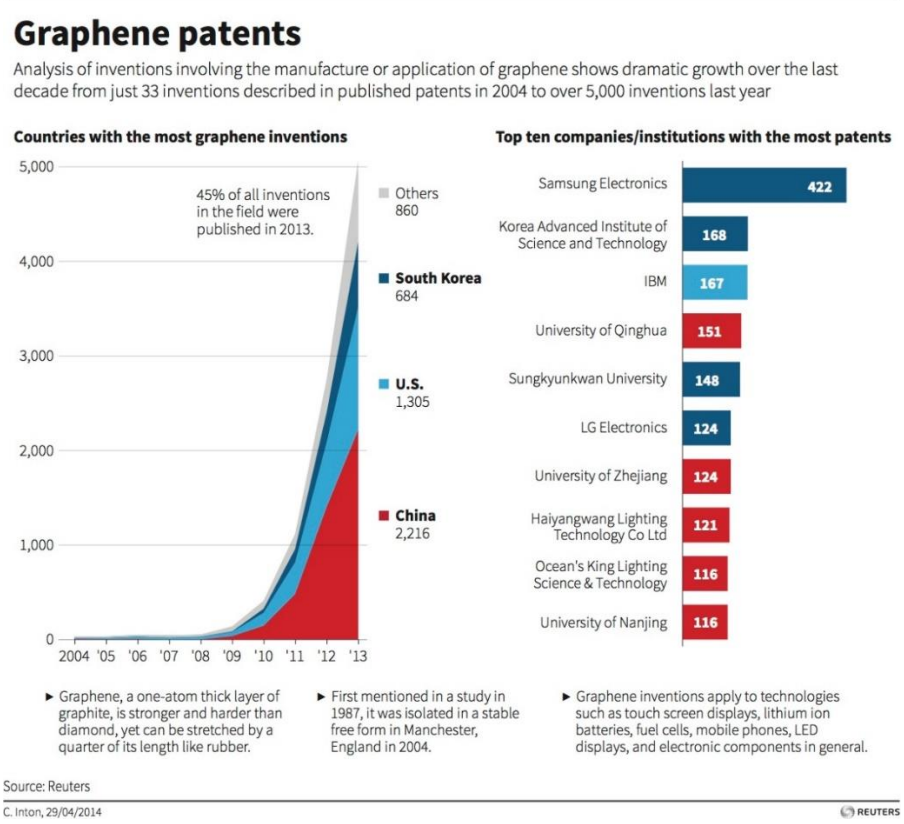

Figure 1-2: Graphene patent trend in a decade since the discovery. [18]

It has no band-gap with infinite Bohr radius that imparts metal-like conductivity in graphene sheets, thus possibility of confinement for any finite size of graphene[24]. Figure 1-3 shows the historical timeline towards the discovery of exfoliated graphene by Geim et al.

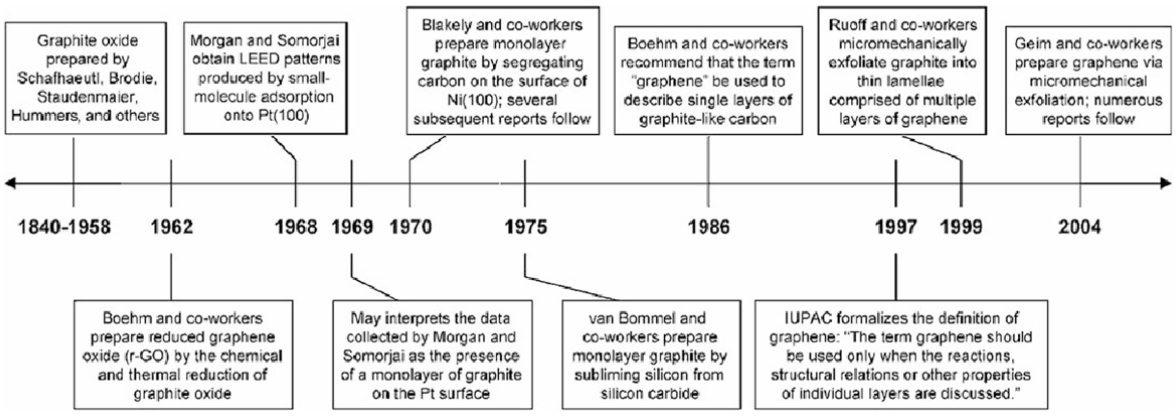

Figure 1-3: A timeline of selected events in the history of graphene for its preparation, isolation and characterization. Reproduced from Ref. [25] *with permission from Wiley*

1.2.1 Synthesis of Graphene

Graphene synthesis is one among the most heavily researched issues. The search for the right method to get high quality large area graphene finds a major chunk of research in most cutting edge research laboratories. As a result many physical and chemical methods have surfaced for graphene synthesis, based on mechanical or chemical exfoliation of graphite[26], unzipping of CNTs[27], chemical reduction of GO[28], CVD or epitaxial growth[29,30]

1.2.1.1 Mechanical Exfoliation

Dry mechanical exfoliation is the most popular as well as efficient methods for extracting single or few layer graphene[31]. The adhesive tape based process involves a simple graphite peeled off repeatedly and transferred on desired substrate[2] also called the scotch tape method. Although easy, yet time consuming process with low yield and low reproducibility at least cost. The process does not necessarily provide a good quality graphene, which may get damaged during repeated peel off steps.

1.2.1.2 Chemical exfoliation

A high-yield solution based process with better reproducibility at low cost is chemical exfoliation of graphite by Ultrasonication and intercalation before centrifugation[26,32]. This involves use of inorganic salts such as $(NH_4)_2SO_4$, Na_2SO_4, K_2SO_4[26] or water-surfactant solution, sodium cholate[33]. The centrifugation step segregates and helps select the largest graphene exfoliated during the exfoliation process. The ultrasonic cleavage is strongly dependent on the choice of solvents used with surfactants and ultrasonication parameters such as frequency, amplitude and time [34].

1.2.1.3 GO reduction

Graphene oxide GO can be prepared by a number of routes. Graphene oxide synthesis by Hummers method involves graphite soaking in H_2SO_4 and $KMnO_4$.The resulting graphite oxide is sonicated to obtain single layer GO. Finally GO is reduced with suitable reagents to form reduced graphene oxide rGO[35,36]. The use of acids renders structural defects on graphene. The graphene obtained by GO reduction is different from pristine graphene. This method is scalable, time efficient and economic despite reduction borne defects caused by reducing agents involved in the process.

CVD graphene

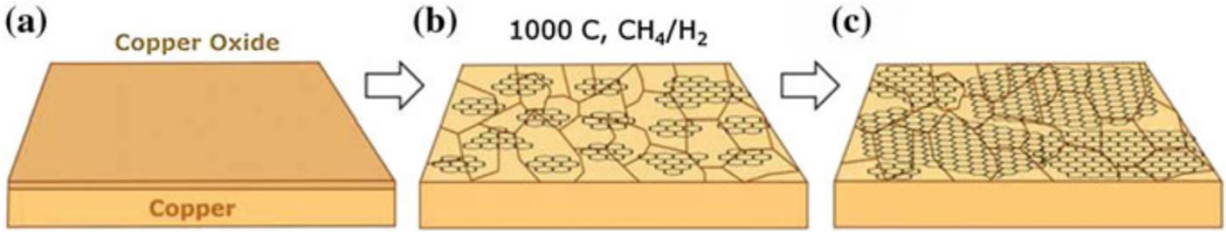

Figure 1-4: Schematic CVD based graphene synthesis. a) Deposition of copper thin film with native oxide; b) Exposure of Cu to CH4/H2 at 1000 oC; c) The graphene nucleated in previous step grow into graphene flakes. Reproduced from Ref. [37] with permission from The Royal Society of Chemistry

The schematic in Figure 1-4 illustrates typical CVD growth of graphene. CVD grown graphene is most efficient yet expensive method for graphene synthesis as it gives large surface areas with uniform and high crystal quality at large manufacturing volumes[38,39]. Copper has least affinity and low carbon solubility compared to other transition metals (Co, Ni) towards carbon which makes it best candidate for catalyzing CVD graphene growth In a recent research up to 0.5 mm single crystal graphene was grown on copper foil by low pressure CVD[40].

1.2.2 Applications

Like any other material, graphene has been researched for applications in all walks of life, but compared to others, graphene has aced all the tests. Both public and private investments have fueled graphene research to graphene commercialization and applications. The market based products have already started to show up in form of tennis rackets, battery strap by Vorbeck, or the touch screen phones by Samsung. The size of graphene market has steadily increased alongside a surge in graphene patents as shown by Figure 1-2. In the meantime graphene applications classified by technological readiness as shown in, Figure 1-5 elaborate the current state and futuristic applications chalked out for graphene. Graphene is on the verge of being taken up as the material of choice for a variety of applications in futuristic products. In field of plasmonics, being ultimate thin 2D material, flexible and inert material which can be fabricated and patterned by standard silicon based clean room systems. Graphene plasmons are tunable either by electrostatic or chemical doping compared to noble metal counterparts[41] and can extend into NIR and MIR regions of electromagnetic spectrum. Graphene sheets have been used to compose solid 3D networks of graphene sponges, foams, templates, and aerogels that exhibit high surface area, strength, accessible pore volume and high conductivity even at very low density[42]. Ahmad et al

reported graphene nanoribbon arrays for high performance NO_2 sensing applications down to 20 ppb.[43]

Xu et al reported self-assembled 3D Graphene macrostructures for super capacitor applications [44]. Liquid phase exfoliated graphene as filler material in phase change materials has shown promise for thermal management of high power battery packs[45]. Among other photonic applications, it has been used for solar cell [46], graphene plasmonics[47], graphene based flexible OLEDs[48]

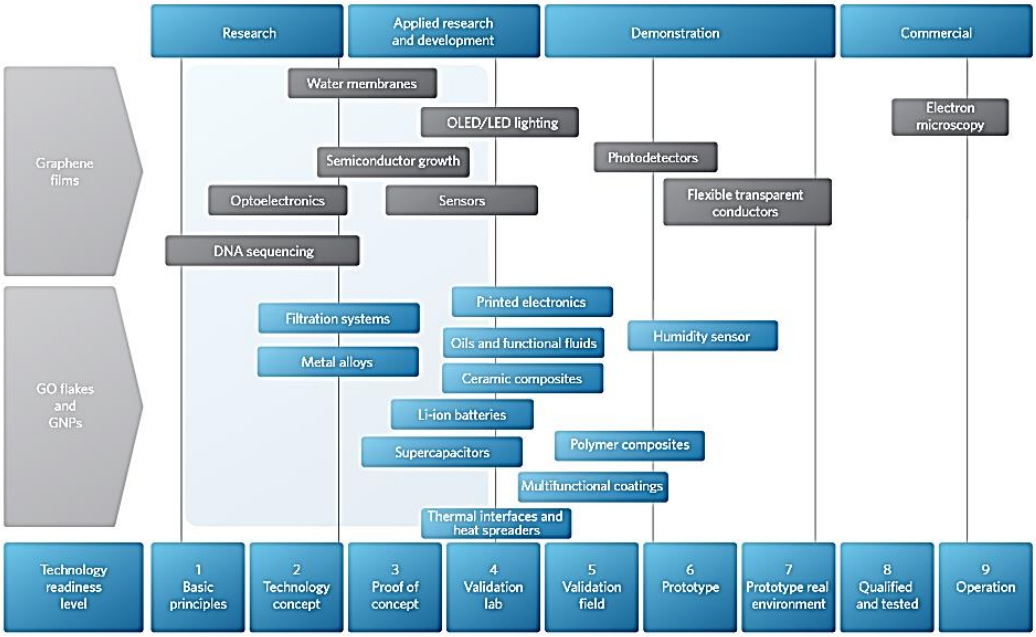

Figure 1-5: Graphene applications classified by technology readiness level. Reproduced from Ref [41]

photodetector[49] and encapsulations[50]. Graphene has also been used in super capacitors[51,52], energy storage[53,54], memory[55] and many other applications.

1.3 Graphene Quantum Dots

Band-gap induced graphene in form of graphene quantum dots (GQDs) and nanoribbons have found great interest in recent years. GQDs are the zero dimensional sp^2 hybridized carbon systems, same as the three dimensional (3D) structure in the case of graphite, 2D graphene, or one-dimensional (1D) carbon nanotubes. Graphite is in fact multi-stacked graphene, whereas carbon nanotubes (CNTs) are graphene sheets rolled up into cylinders. GQDs are typically smaller than 20 nm in diameter [56] comprised of single or multilayer graphene. GQDs have numerous proven applications in bio imaging [57] and photonic devices such as solar cells [58], photodetectors[59], light emitting diodes [60] and many others due to the altered quantum confinement and presence of edge states[61]. GQDs are often synthesized by breaking materials comprised of 2D graphene sheets into 0D nanostructures. Compared with carbon dots, GQDs also have higher surface to volume ratio and the remarkable, graphene structure, hence providing them with comparatively superior properties.

1.3.1 Synthesis

There are various methods for GQD synthesis that can be divided into two major approaches: top down and bottom up approaches. Top down approaches involve the breaking down of mesoscopic 1D, 2D or 3D graphene structures such as CNTs, graphite, graphene platelets, carbon fibres or carbon black[62] into smaller fragments by hydrothermal [63], solvo-thermal [64], electro-chemical [65], microwave assisted hydrothermal [66] or nanolithography [67] to smaller fragments. The hydrothermal route involves separate graphene oxide cleaving and reduction processes, which require up to three days [68]. In bottom up approaches, such as hexaphenylbenzene pyrolysis [69], tetra-phenyl-cyclo-pentadienones and diphenyl ether reflux under argon atmosphere [70] or laser exposure of benzene [71] and compounds containing fullerenes like polycyclic aromatic molecules are used to synthesize GQDs. Most of these methods either use acids [72,73] or high temperature treatments during synthesis.

It is highly desirable to improve the synthesis of GQD with a desired size by minimizing the need for expensive equipment, high temperature process, and highly caustic and hazardous chemicals. In this study, a direct ultra-sonication assisted GQD synthesis approach was developed, which involves grinding and ultra-sonication in the presence of two solvents without the use of any acidic reagents [72,73], high temperature treatments, or sophisticated apparatus [71,74].

1.3.2 Applications

The graphene quantum dots were used as green and facile sensor for free chlorine in drinking water, thus envisioned for likely applications for drinking water [75].

1.4 Graphene Nanocomposites

Nanostructured materials behave in an altogether different way when compared to their bulk counterparts. In last decade nanotechnology has become steadily richer for fabrication of nanostructures. The zero, one and two dimensional materials have been used to impart new properties for improving device characteristics, which were thought impossible in bulk form. Graphene has been the revolutionary two dimensional (2D) carbon containing benzene like repeating unit cell, with single atom thickness [5]. It has proved to be revolutionary material for many novel applications such as photonics[76], plasmonics[77] and as transparent electrode material [78]. It has also been utilized in the form of composite with metallic nanoparticles [79], nanowires [80], and polymers for enhancing their shortcomings [81]

1.5 Resistive Switching

The structure of a memristor is similar to a capacitor, as an insulating material is sandwiched between two metal electrodes as shown in Figure 1-6. This structure is also known as metal/insulator/metal (MIM) structure.

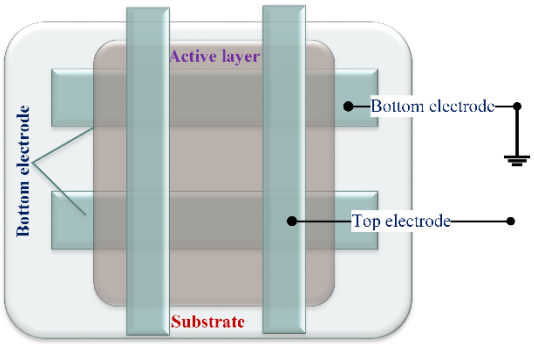

Figure 1-6: A schematic of sandwich structured resistive switching device.

There are many electrically induced resistive switching effects as illustrated in Figure 1-7. The nascent active layer in a memristor has a high resistance. An electrical voltage is applied to set off a process called electroforming voltage. Generally speaking, resistive switching in a memristor occurs on passage of suitable magnitude of electric current through thin film of an active material.

The resistance of the film can be switched back and forth, between a high resistance state (HRS), "OFF" state and a low resistance state (LRS), or "ON" state [82].

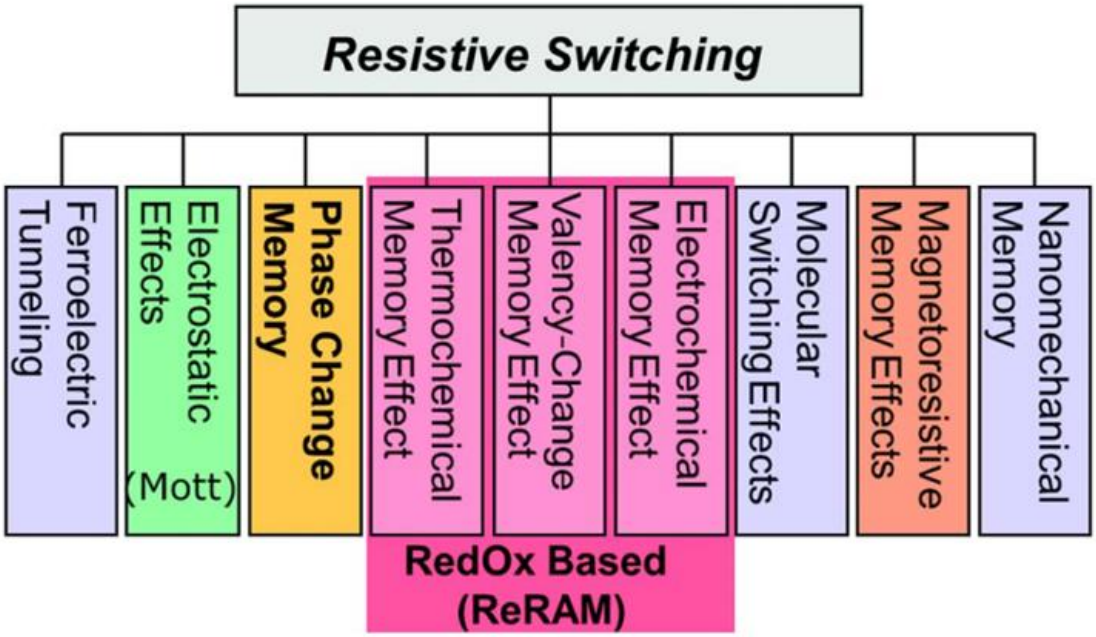

Figure 1-7: Taxonometry of Resistive Switching memories (schematic adapted from [83], reproduced with permission).

This switching is attributed to thermal, electronic and/or ionic effects [84]. The thickness of the active layer in the sandwich structure configuration has been reported from ~2 nm to several hundred nanometers. The core memristor attributes such as its conduction and switching mechanism, working speed, resistance ration in off and on states depend on the active layer. Ever since 1960s, researchers have explored various metal sulfide[85], organic[86,87], oxides of both metals[88] and non-metals[89] and phase change materials[90–92] as active layer. Many high dielectric constant polymers have been studied for memristive behavior. Poly(4-vinlyphenol) (PVP) finds application as dielectric in thin-film transistors (TFTs)[93,94], resistive switching and write-once read-many (WORM) memories [95]. Several polymer/nanoparticle [96,97] memory devices have been reported. The change in memristive behavior of PVP, in presence of graphene flakes, has been reported in our previous study[98].

1.5.1 Resistive switching mechanisms

The switching mechanism depends on the sandwich structure, the electrodes used as well as the mode of operation of the resistive switching device. The switching mechanisms can be classified

into five types. Ion migration, charge trapping/detrapping, thermochemical reaction, and the exclusive mechanisms for organic and inorganics. The ion migration mechanism requires an electroforming process whereby triggering stable RS behavior. The local rupture and reformation of the conducting filament (CF), reset and set the RS states, and switch between HRS and LRS. These ions can be cations or anions depending on the nature of electrodes and the active material used. The active electrode and the counter electrodes The CF are formed via electrochemical dissolution and latter redepositing active metal atoms. In case of Ag active electrode (AE) positive bias during electroforming and set steps undergo the anodic dissolution at the electrode, then migration of the Ag^+ ions along grain boundaries towards counter electrode (CE) followed by the reduction of Ag^+ ions and the growth of filaments. The device switches from HRS to LRS as soon as the filament short circuits the two device through the CF. The existing filament however does not sustain the joule heating along its thinner parts and ruptures the memory element back to the HRS. In 1976 Hirose[99] reported was first to study Ag/Ag–As_2S_3/ Mo sandwich structure and report the bipolar RS behavior. The range of materials reported until now has grown steadily to include oxides such as ZrO_2[100], GO[101,102] and ZnO[103,104], as well as polymers such as PVP[105,98,106], P3HT[107] and many others. The charge trapping/detrapping mechanism based memristors trap the charge carriers injected from electrodes in form of space charge. It then modulates the carrier injection and/or affect their flow through the active layer. The mechanism can be classified in three groups. The interfacial charge traps occur in case of Schottky junction formation that get altered by application of external electric fields. The charge traps may also occur within inorganic or organic active layers.in form of nanoparticles[108], graphene film[55] or quantum dots. The third category involves randomly distributed charge traps such as Au or Ag nanoparticles[109] carbon nanotubes[110] or graphene flakes[105,98].In semiconductors memristors the forming and set processes occur by thermal decomposition of active layer and subsequently the CF formation whereas the reset process is caused by thermal meltdown of CFs formed during set process. The thermochemical reaction mechanism mediated RS has been reported for Pt/NiO/Pt [111] and Pt/ZnO/Pt[112]. VO_2[113] and NbOx[114] studies have demonstrated insulator to metal transition from the field induced joule heating effect. The mechanism is responsible for nonvolatile RS behavior in VO_2. The amorphous carbon RS studies has also shown similar process[115]. In case of polymers and organics the charge transfer as a consequence of external field is due to donor and acceptor moieties existing within

the active layers. For a PVK-C_{60} [116]polymer based memristor charge transfer between carbazole and C_{60} demonstrated by 100:1 shows bipolar RS behavior upon sandwiching between Al and ITO.

1.5.2 Applications of memristor

Although mostly studied for memory applications, memristors have been studied for logic circuit, unconventional computing, spintronic, photo electronics, etc[117–120].

1.5.3 Types of Resistive Switching

In general, two switching schemes are prevalently reported and distinguished by the current-voltage (I-V) characteristics as shown in Figure 1-8. A voltage polarity dependent process is known as unipolar, whereas its voltage polarity independent counterpart is known as bipolar switching.

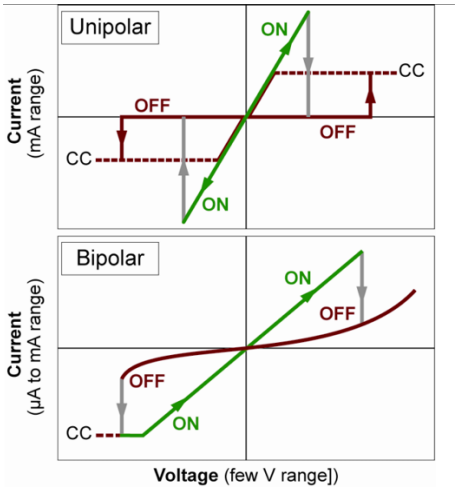

Figure 1-8: Unipolar and bipolar switching schemes. CC denotes compliance current, often needed to limit the ON current. (adapted from[84], reproduced with permission)

In the case of bipolar switching the SET to ON and RESET to OFF states occur on opposite voltage polarities. In either of these characteristics, the reading voltage, V_{READ} to read the state is usually small so that it does not affect the state as shown in Figure 1-8.

Chapter 2. THIN FILM FABRICATION PROCESSES

2.1 Conventional Thin Film deposition Processes

Printed electronics industry now stands as a major contributor to human advancements and futuristic innovations such as 3D and 4D printing are already paving way for further advancement of human civilization. Printed electronics mostly deals with ability to print the whole device in batches so that costs are minimized with high end products into flexible and stretchable electronic applications. Thin film fabrication has been one most significant processes in nanotechnology. Conventional vacuum based processes employ various low to ultra-low vacuum for thin film fabrication. They include but are not limited to physical vapor deposition[121,122], chemical vapor deposition[123–127], sputtering[128–130], electron and ion-beam evaporation[131–133], molecular beam epitaxy[134–137], laser ablation[138–140], plasma[141–143] and atomic layer deposition[144,145]. These processes have matured over the years and can give very high quality thin films of required materials over a variety of thicknesses. Recently the non-vacuum thin film fabrication technology has started showing promise. The advantages among others are low cost, less time consuming and batch process-ability. The solution processible colloids and inks market is on the move. The demand for room low temperature material processing is mainly driven by research for flexible and stretchable electronics. One method very common for solution processible thin film fabrication is spin coating, employed mostly for proof of concept devices. Processes such as dip coating, slot die coating, inkjet printing, electrohydrodynamic atomization[60,146–151] have been employed for thin film fabrication at room temperature without the requirement of vacuum. The thin films fabricated by these techniques have been used in solar cells[152], photodetectors[153], memristors[105], nanogenerators[154] and supercapacitors[155–157], which evidently proves, the viability of these techniques in printed electronics industry. The patterning of structures is just as important as thin film fabrication in an electronic device. Roll to Plate, screen, gravure, offset gravure, and electrohydrodynamic printing have been promising techniques that work efficiently well at room temperature and atmospheric pressure

2.2 Electrohydrodynamic Atomization (EHDA)

Electro-hydrodynamic atomization (EHDA) has been a preferred low-cost, non-contact, and efficient material printing technique that can be used in a variety of ways for layer by layer

deposition of materials. The details of EHDA phenomenon has been elaborated in detail by Poon [158] and has been used for fabrication of thin film device applications[159–162], OLED[60], thin film memristor[105] and Schottky diodes[160]. EHDA process optimization is carried out by carefully adjusting the operation parameters, such as the stand-off distance, operating voltage between the metallic nozzle with respect to grounding terminal, the diameter of nozzle, the conductivity and viscosity of the ink used, and the ink flow rate. The thickness of the thin films deposited by this process can be optimized either by varying number of passes or by controlling the speed of translation of needle across the target substrate. As in case of deposition of thin film deposition of Graphene nanoflake/PVP[105] nanocomposite by EHDA, the in-house built EHDA system[147,159,163,164] fitted with a metallic capillary nozzle of a suitable inner diameter of 310 um (Havard 33G) was used. The schematic diagram of the EHDA setup is shown in Figure 2-1(a). The thin films were deposited on top of ITO as bottom electrode, and at the end finished up by a silver top electrode, as an ITO/active layer/Ag MIM sandwich structure schematically shown in Figure 2-1 (b). The prime requirement same as any other thin film deposition process, prior to EHDA of thin films, the as-received ITO coated PET substrates must be cleaned by acetone, ethanol and deionized water in sequence by bath sonication, for 5 min each, at room temperature and dried in air to get rid of any contaminants. Afterwards, the substrates were cleaned by ultraviolet-ozone exposure for 5 min and oxygen plasma treated for 3 min to get rid of organic residues from surface.

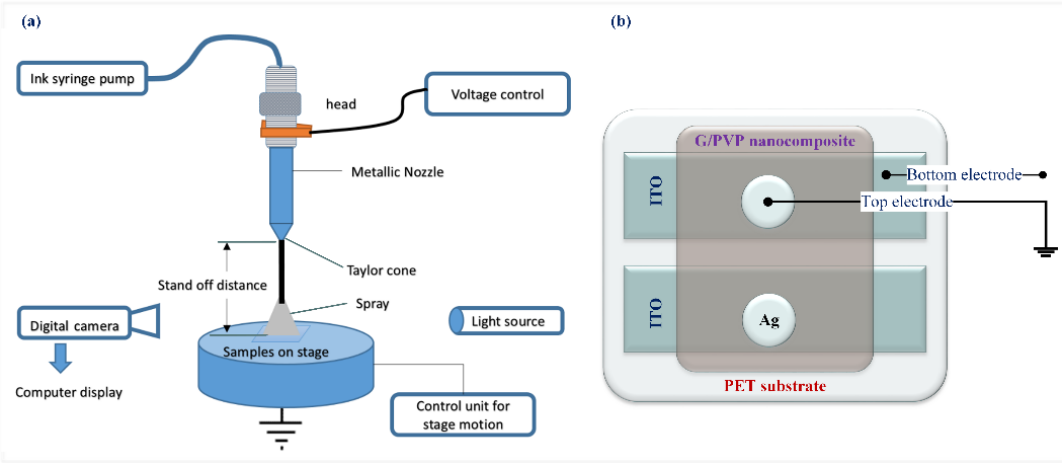

Figure 2-1: (a) Schematic configuration of an EHDA setup for deposition of composite for fabrication of thin films. (b) Device structure and voltage sweep applied across a typical device. The voltage across the two terminals is varied between +3 and –3 V.

Ink (PVP/Graphene nanocomposite in NMP) was fed to the liquid chamber via Teflon tube to nozzle by a syringe pump (Hamilton Model 1001 GASTIGHT syringe). The flow rate was controlled by using the pressure control system. An overall operating envelop for composite ink, was established by varying flow rates (50—900 µl/h) and applied potentials plotted in Figure 2-2.

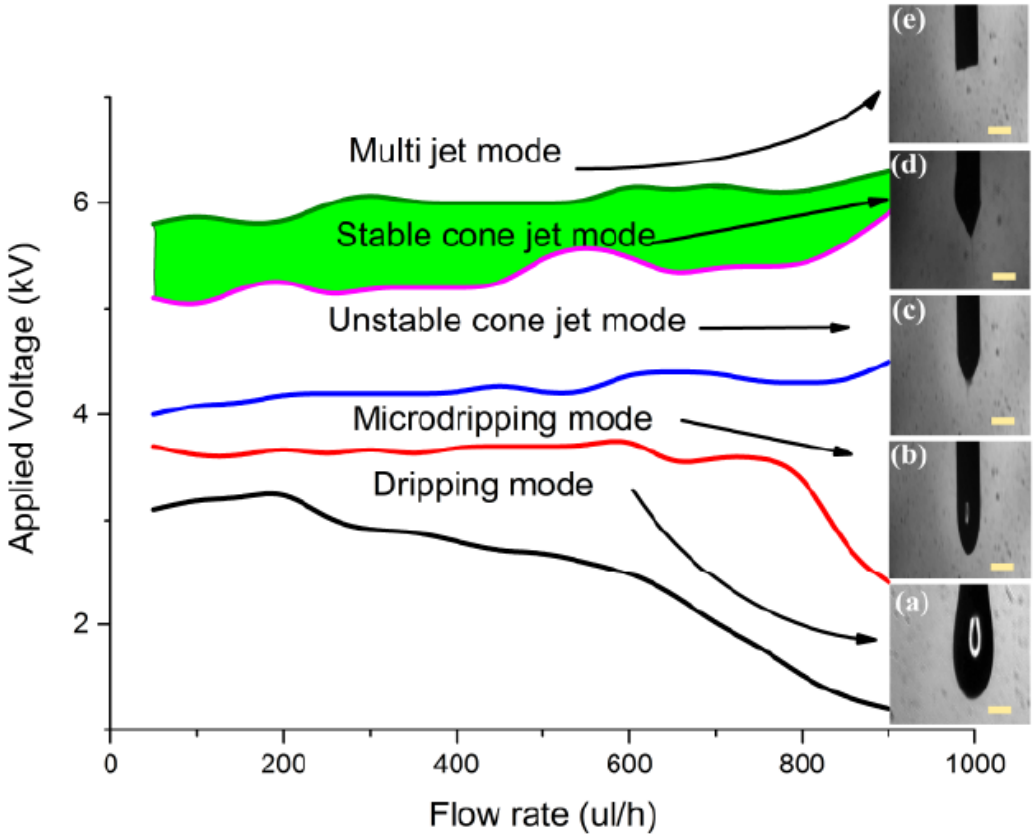

Figure 2-2: EHDA Operating envelop of Graphene/PVP composite. Insets (a)-(e) show the photographs of the jet in different modes. The stable cone jet mode is used for device fabrication

The optimum atomization mode called stable cone jet mode, was achieved at constant stand-off distance of 15 mm between the nozzle and the substrate. The different atomization modes of EHDA process were captured through high speed CCD camera (MotionPro X) Insets Figure 2-2 (a) to (e).

Initially at flow rate of 200 µl/h, a dripping mode appeared from voltage of 3.3 to 3.7 kV. Further increasing voltage, micro-dripping appeared and continued until 4.2 kV. While increasing the voltage beyond 4.2 to 5.3 kV, ink emanated from nozzle in unstable cone jet mode. . The desired atomization of ink in the stable cone-jet mode was achieved from 5.3 to 5.8 kV. Beyond 5.8 kV, the jet disintegrated, into the multi-jet mode. The substrate was placed on a computer controlled translation stage, and substrate movement was varied from 1 to 3 mm/s to establish ITO

coverage of about 1 x 2 cm^2 keeping stand-off distance fixed. The film was deposited at translation speed of 3 mm/s and cured at 120 ^oC for 6 hours in order to safeguard the PET from undergoing plastic deformation and evaporate solvent remnants.

Chapter 3. EXPERIMENTAL

3.1 Synthesis of Graphene Nanostructures and Nanocomposites

PVP (average M_W 25,000) powder, poly(melamine-co-formaldehyde), the cross-linking agent, propylene glycol methyl ether acetate and N-methyl-pyrrolidone (NMP), 1, 2-dichlorobenzene (DCB) solvent were purchased from Sigma Aldrich. Graphene flakes (less than four layers and surface area greater than 750 m^2/g) were purchased from Cheap Tubes.

3.1.1 Graphene Flakes

Graphene flakes are graphene microstructures with lateral size in a few microns yet keeping single to few layer graphene in their structure.

3.1.2 Synthesis of Graphene Nanoflakes

The synthesis of a precursor solution for the EHDA is a critical benchmark for achieving the uniform thin film deposition [165]. Graphene nanoplatelets dispersion was synthesized[149] by dispersing graphene nanoplatelets (0.8 mg) in NMP (10 ml) by bath sonication for 15 min. This dispersion was subject to 2 hours of violent shaking by mechanical shaker and also 2 hours of stirring by a magnetic stirrer. To improve exfoliation and further the prospect of breaking the graphene flakes down to even smaller size [166], the dispersion was bath sonicated for 6 hours at room temperature and probe sonicated for 1 hour. The ultrasonic energy transferred during this step increased temperature of water in the sonication bath. This rise in temperature was kept in check by consistent replacement of ice packs every 30 min. Only the top 75% supernatant in vile was extracted after centrifugation at 4000 RPM for 30 min. The supernatant was first filtered by using syringe filter (Whatman polypropylene) of pore size 0.45 µm and later by another filter of pore size 0.2 µm to remove any large size flakes remaining in solution. Thus after first filtration through 0.45 µm filter the largest flake to pass though the filter was ~450 nm. Thus lowering load and avoiding clogging of 0.2 µm pore size filter by the larger flakes.

The Graphene flake size reduction was assessed by employing a Cs-corrected Spherical Aberration Correction Scanning TEM (JEM-ARM 200F), operated at 200kV. The success of the process is evident from the TEM analysis of these graphene flakes performed after sonication step. The processed graphene was analysed by TEM to confirm size reduction evidently shown in Figure 3-1 (a). The high resolution TEM image in Figure 3-1(a) shows that the flake size reduced to even smaller nanoflakes with average diameter of about 20 nm. Figure 3-1 (b) also reveals single to few

layer graphene, showing successful exfoliation of multilayer graphene flakes. Figure 3-2 shows synthesis of graphene nanoflakes from graphene flakes by processing steps mentioned above.

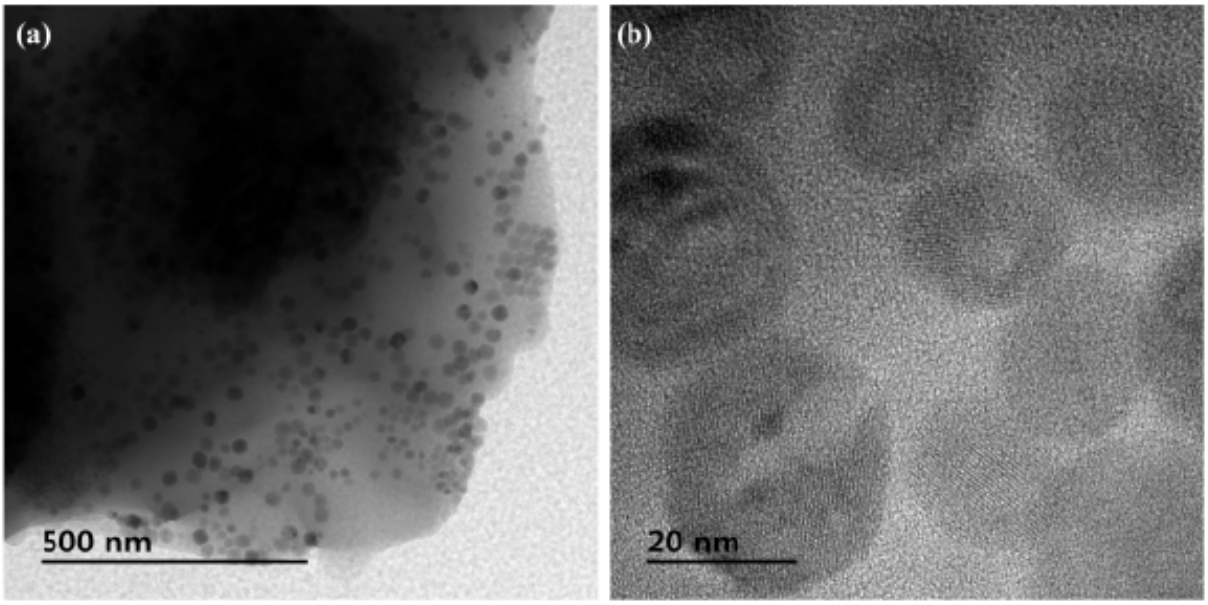

Figure 3-1: (a) High and (b) low magnification TEM images showing the nanosized graphene flakes after processing. The minimum size of these nanoflakes is ~20 nm.

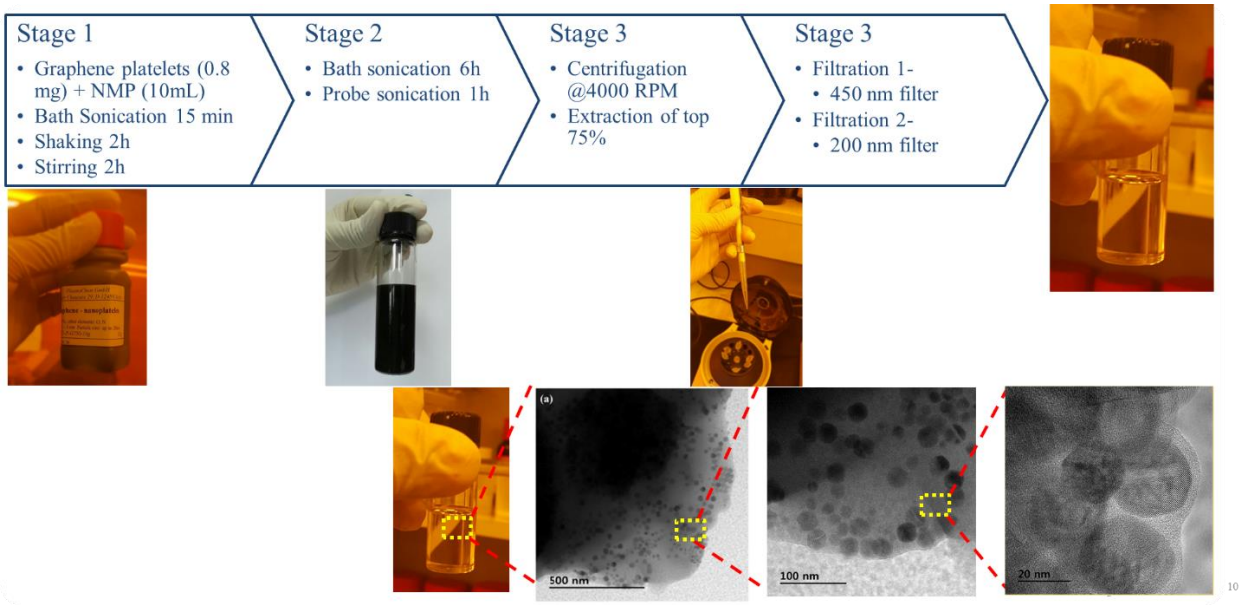

Figure 3-2: Synthesis of Graphene nanoflakes from graphene flakes. The size of Graphene flakes as observed by TEM analyses

3.1.3 Synthesis of Graphene Quantum Dots

Graphene flakes were purchased from Cheap Tubes (44 layers and surface area 750 m^2/g), and N-methyl-pyrrolidone (NMP) and 1, 2 dichlorobenzene (DCB) were purchased from Sigma Aldrich. All reagents were used as received without any further purification. First, 120 mg of graphene flakes and a few drops of NMP were poured in a mortar and then ground for 360 minutes using a pestle. The NMP was added to keep the powder moist to assist in grinding and exfoliation. The ground graphene was then dried at 100 ℃ for 1 h, and the powder was extracted and weighed for further processing. Next, 10 ml NMP, 10 ml DCB and 100 mg ground and dried powder were added in a cleaned bottle. The three were mixed thoroughly with a magnetic stirrer for 1 h at 1000 rpm at room temperature, followed by mechanical shaking for 4 h at 300 rpm. After mixing, the product was sonicated in an ice pack filled water bath for 4 h at room temperature. A Fisher Scientific Sonic Dismembrator (100 W) was used for ultra-sonication for 1 h to break the graphene sheets into even smaller fragments. The supernatant was collected after centrifugation for 30 min, using a WiseSpin (CF-10) at 5000, 8000, 10000 and 13500 rpm rotation speeds, named as samples S-1, S-2, S-3, and S-4, respectively. The supernatants were dried by evaporation of the solvents in air at 100℃. Finally, the dried GQD powder was used for XRD and Raman characterizations.

The GQDs were prepared by a sonication-assisted mechanical method. This approach involved first grinding few layer graphene flakes (GF) for 360 min in presence of N-Methy l-2-pyrrolidone (NMP) to assist the exfoliation process, as well as to break down the flakes to smaller sizes [167]. Afterwards, violent shaking and ultra-sonication in the presence of 1,2 dichlorobenzene (DCB), in addition to NMP, helped further break down the graphene to even smaller fragments[168,169]. DCB has already been reported as a good organic solvent for exfoliation of graphene[170]. Figure 3-3 shows the flow diagram of the proposed chemo-mechanical process. The last stage of the process was centrifugation at high rotational speeds. Only supernatant species were collected for further characterization, since the sediments were expected to have a wide range of graphene sizes [171]. The processed GF, collected before and after centrifugation have been shown in Figure 3-3. The colour change from opaque black to transparent golden yellow is clearly depicted in the photographs of the GQD sample before and after centrifugation. The flakes were broken down into smaller fragments during the chemo-mechanical treatment. The presence of NMP helped exfoliate the graphene, whereas the DCB was helpful for unzipping and the extraction of the GQDs.

Transmission electron microscopy (TEM) investigation of unprocessed graphene flake in Figure 3-4(a) shows few to single layer graphene sheet with long range crystalline order. whereas the selected area electron diffraction pattern in Figure 3-4(b) shows the characteristic crystalline graphene [172,173]. The surface scan histogram Figure 3-4(c) evaluated from the high resolution TEM image of GF shows lattice parameter of 0.24 nm in agreement with literature [174]. TEM

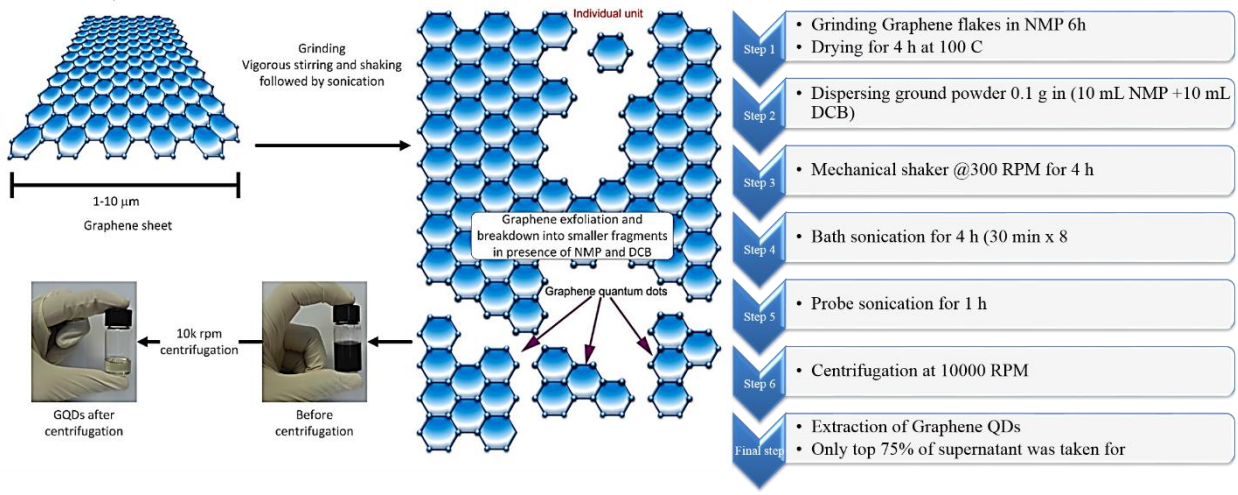

Figure 3-3 Schematic of Graphene QD synthesis by the co-solvent, grinding and ultra-sonication-assisted mechanical route. The graphene sheets were broken down initially by grinding, and then through ultra-sonication in the presence of NMP and DCB. The supernatant species extracted as a result of centrifugation showed a transparent golden yellow color compared to the opaque char black for chemo-mechanically processed graphene before centrifugation.

investigation was carried out for samples, S-1, S-2, S-3, and S-4, obtained after final centrifugation at 5000, 8000, 10000 and 13500 rpm respectively for 30 min as shown in Figure 3-5(a). Nano-Measurer 1.2 was used for calculating the diameters by analysing the TEM images of each sample. The insets show the high resolution TEM of individual GQDs from each of the four samples with lattice spacing of 0.24 nm and highly crystalline structure. 2D FFT pattern (shown in inset) of the TEM image of one of the GQD samples also validated the presence of the characteristic hexagonal graphene structure [175]. The average diameters of the GQDs collected after various centrifugation speeds have been tabulated in Table 1.

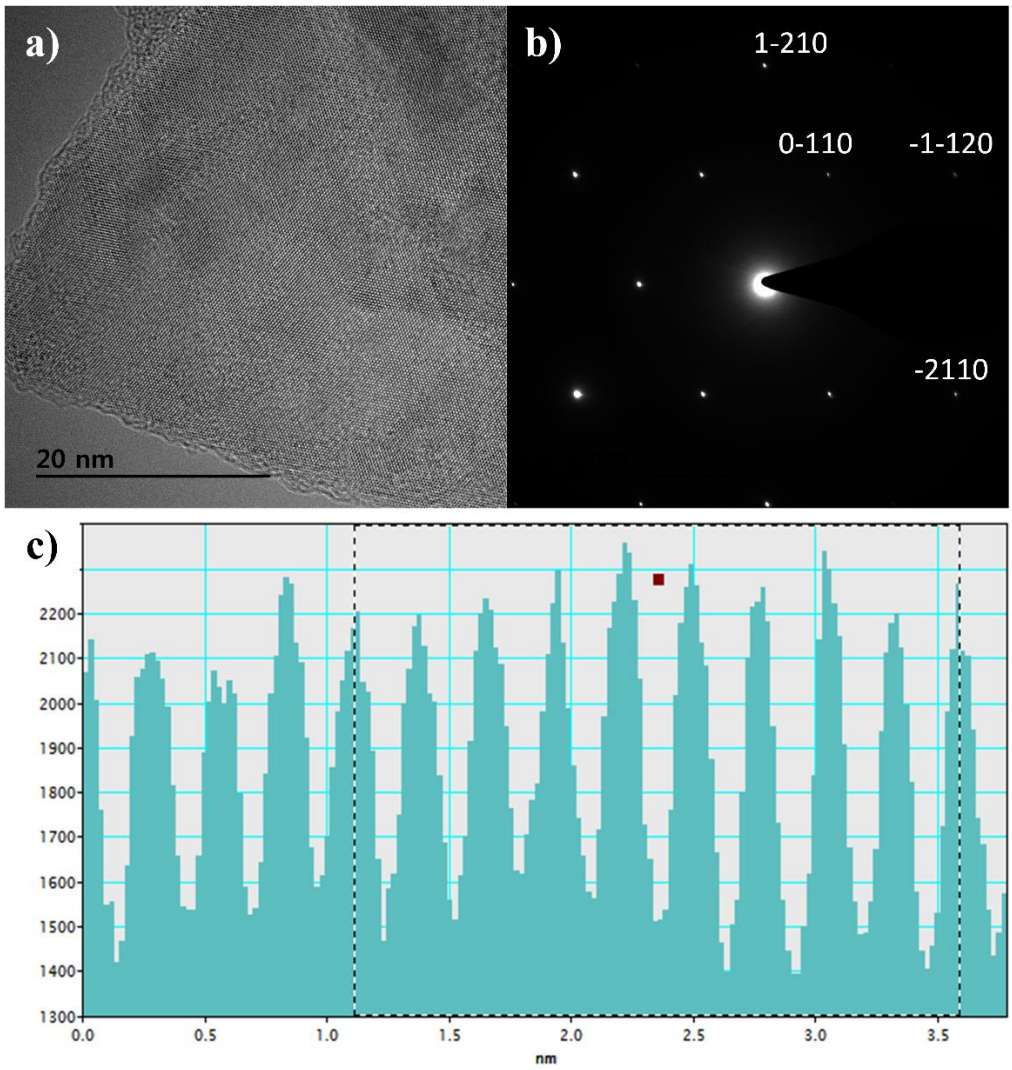

Figure 3-4: (a) HRTEM analysis of graphene flake in the sediment after processing shows crystallinity. b) The SAED pattern shows six-fold symmetry for graphene crystal structure, and c) the 2D surface scan profile shows the characteristic lattice spacing of about 0.24nm.

Table 1: Relation of centrifugation speed with diameters of extracted GQDs. It is evident from the table that variation in centrifugation speed yields change in the GQD diameters.

Sample	Centrifugation Speed (rpm)	Diameter (nm)
S-1	5,000	3.92 ± 1.09
S-2	8,000	3.04 ± 0.83
S-3	10,000	2.62 ± 0.68
S-4	13,500	1.96 ± 0.43

The size distribution of the extracted GQDs obtained by variation of centrifugation speed is shown in Figure 3-5(b). Diameters of 200 GQDs spotted from TEM images were calculated for each sample. The average size of GQD in S-1 was 3.92 ± 1.09 nm, the largest among the 4 samples. The average GQD diameters for S-2 and S-3 were 3.04 ± 0.83 nm and 2.62 ± 0.68 nm, respectively. Sample S-4 had the smallest GQDs among the four, with an average size of 1.96 ± 0.43 nm, and also showed the narrowest distribution compared to the samples centrifuged at lower speeds. All samples accorded well with Gaussian distribution. The change in diameters of the extracted GQDs showed an inverse relation with the centrifugation speed, as shown in Figure 3-6. Thus, it was inferred that it is possible to extract GQDs of the desired size from the supernatant by controlling the centrifugation speed [166]

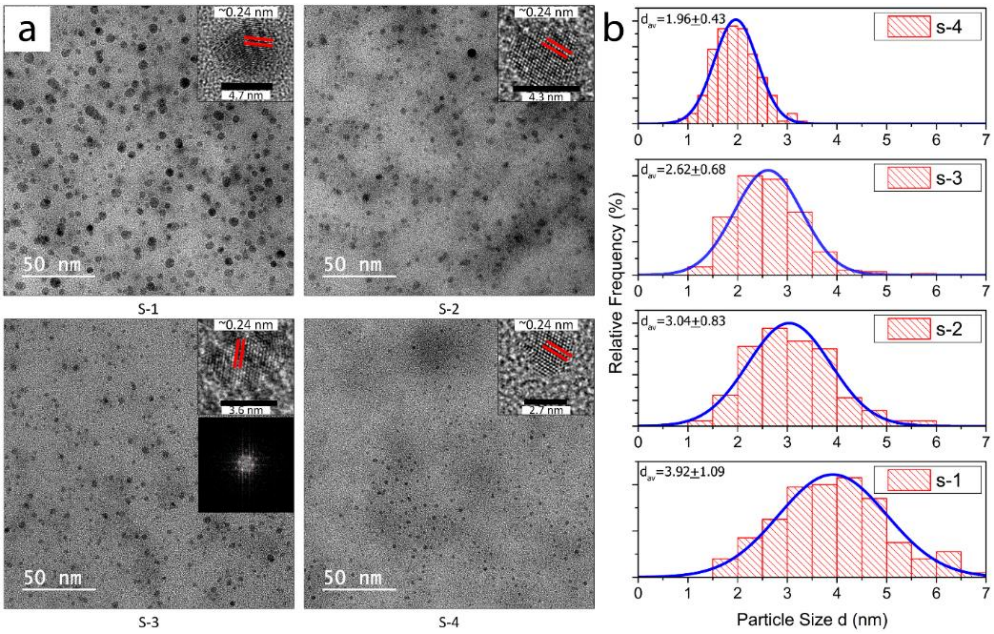

Figure 3-5: a) TEM images of GQDs extracted at different centrifugation speeds: S-1 at 5000, S-2 at 8000, S-3 at 10000 and S-4 at 13500 rpm. The insets show respective HRTEM images of the GQDs from each sample, showing 0.24 nm lattice spacing. The 2D FFT of the GQD TEM image also showed the six fold rotation symmetry for the graphene lattice, and also provides evidence of crystallinity. b) The diameter distribution of the extracted GQDs samples S-1 through S-4. Diameter distribution in each sample agrees with Gaussian distribution. The average QD size in each GQD sample decreases appreciably, from about 4 nm @ 5000 rpm to about 2 nm @ 13500 rpm centrifugation, performed for the 30 min for each sample.

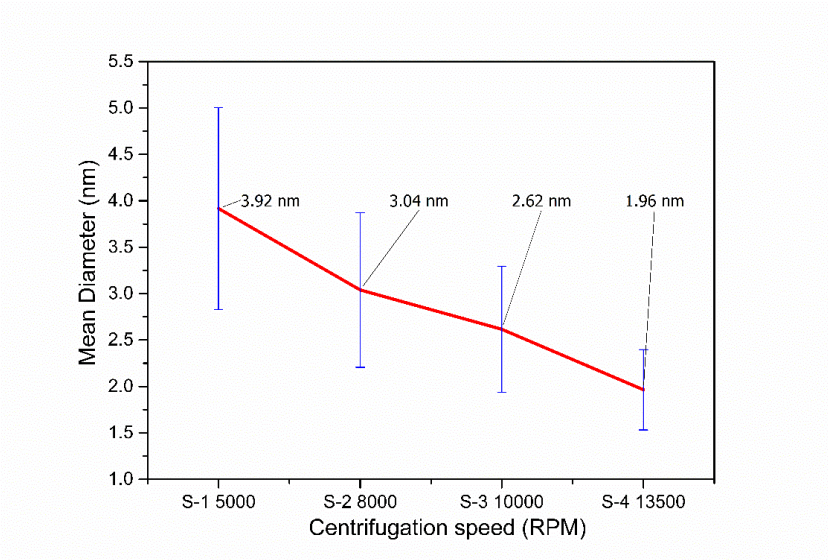

Figure 3-6: The change in GQD diameter with centrifugation speed is plotted, showing a decrease in average size and increase in homogeneity of the GQDs extracted at high centrifugation speeds. The average GQD size in the case of the fastest centrifugation of 13500 rpm

The solvents from sample S-3 were evaporated and GQD powder was collected for XRD and Raman spectral analyses, to confirm the quality of as-prepared GQDs. The Raman spectra Figure 3-7(a) of GQDs reveal the existence of the D band at 1353 cm^{-1} corresponding to the disorder-induced phonon mode. This band involves iTO phonon around the K-point like the 2D band[176]. The G band at 1591 cm^{-1} corresponding to Raman-allowed E_{2g} phonon mode of vibrations was observed due to existence of graphitic structures[71,177]. The ratio of peak intensities for the D and G bands I_D/I_G of graphene-containing species determines the graphene crystallinity. The I_D/I_G determined from the Raman peaks was about 0.88, Raman spectroscopy confirms the quality of the as-prepared GQD in powder sample [178,179]. A typical X-ray diffraction (XRD) profile for synthesized GQD is shown in Figure 3-7(b). The 2θ diffraction peak at 25° corresponded to the 002 peak of graphitic structure. The diffraction peak was in the range of 21° to 29°. The size and

orientation of the GQDs in the powder sample increased the peak width. The d spacing for the GQDs powder was calculated to be 3.4 Å , using the relation $d \sin\theta = n\lambda$, was in good agreement with the reported values (3.40-4.81) [73].

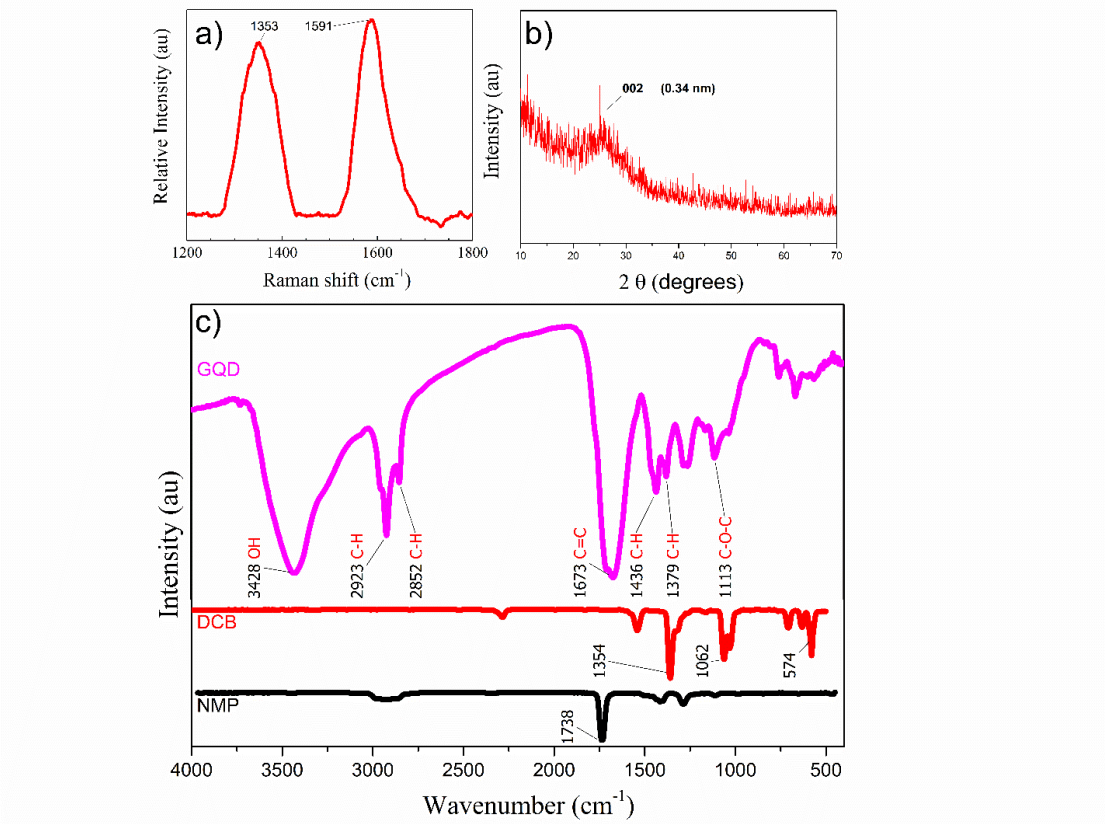

Figure 3-7: a) The Raman spectrum of GQD powder extracted after evaporating the solvents from the GQDs of sample S-3 at 100 ℃. The ratio of the intensities of the D band at 1321 cm^{-1} and the G band at 1590 cm^{-1} was about 0.73, which provides evidence of crystallinity within the GQD graphene phases. b) The XRD profile of GQD powder extracted after drying out the NMP and DCB shows a wide 002 peak at around 25°. c) Comparison of the FTIR of NMP, DCB and GQD powder sample shows complete evaporation of the solvents. The absence of a strong peak at 1742 cm^{-1} from NMP and at 1358 cm^{-1} from DCB when compared with the FTIR spectrum of GQD powder suggests the removal of both solvents inform the powder sample.

Here, in the formula '*n*' is the diffraction order taken as 1 for first order diffraction, and λ = 1.54 nm for Cu K_α line. Figure 3-7(c) summarizes the Fourier transform infrared (FTIR) spectroscopy of the GQDs in sample S-3, DCB and NMP, respectively to explore the bonding composition. DCB showed absorption peaks at 578 cm^{-1} for C-Cl stretching, 1066 cm^{-1} for C-O-C stretching, and 1358 cm^{-1} for C-H rocking due to alkanes. The IR spectrum of NMP showed the

characteristic strong carbonyl peak at 1742 cm^{-1}, which was absent in the GQD samples. Comparison with the FTIR spectrum of GQD showed almost complete evaporation of the solvents during powder extraction. An obvious absorption peak cantered at 1674 cm^{-1} [56] was caused by C=C stretching of aromatic rings [71]. The broad peak cantered at 3429 cm^{-1} indicates the presence of hydroxyl species in the sample, which might assist with the solubility of GQDs in water [180]. The peaks at 1380 cm^{-1} and 2924 cm^{-1} showed the presence of C-H on the surface of the GQDs [71], presumably originating from alkyl groups. The 1262 cm^{-1} peak was attributed to the presence of C-O-C.

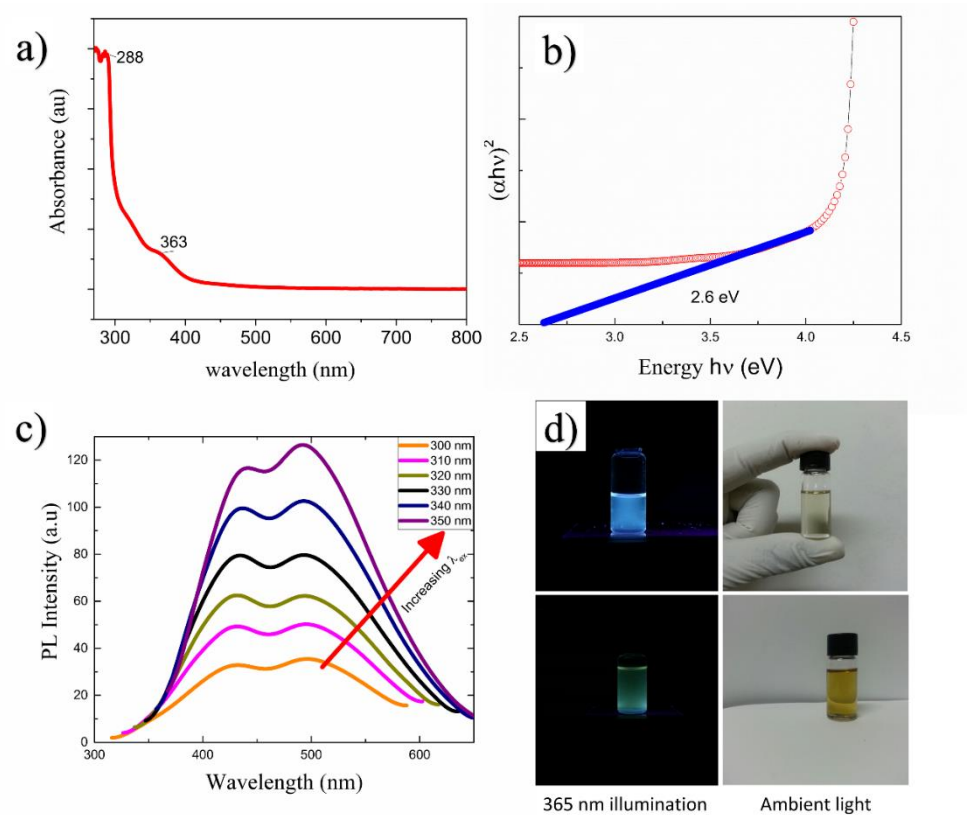

Figure 3-8: a) The UV absorbance spectrum of GQD sample showed strong absorption in the UV region of the electromagnetic spectrum. The absorption subsided in the visible spectrum. b) The energy bandgap calculated by Tauc plot for GQD showed x intercept at 2.6 eV. c) PL properties of the GQDs. The PL spectrum shows twin peaks with strongest emission at 350 nm excitation wavelength compared to 300 nm through 350 nm. d) The GQDs in golden yellow ambient light show blue luminescence for a 365 nm UV lamp illumination. The same sample heated for 3 h at 60 C changes to pale yellow in ambient light and greenish cyan for 365 nm excitation

The UV visible absorption spectroscopy performed on the GQDs revealed weak shoulders at 322 nm and 364 nm [181], as shown in Figure 3-8(a). The GQDs show a broad UV−vis absorption band with a strong shoulder at 289 nm [182] corresponding to $n \rightarrow \pi^*$ transition due to C=O, whereas a hump at 363 nm.

These results are comparable to those obtained for samples prepared by the hydrothermal approach [68]. UV absorption spectra were very difficult to compensate for strong absorption of NMP for wavelengths <265 nm. Therefore the UV absorption wavelengths below 265 nm are not discussed here. The bandgap for GQDs evaluated by Tauc plot as shown in Figure 3-8(b) was about 2.6 eV, which shows promise for application of the GQDs in optoelectronics. The photoluminescence (PL) spectrum was obtained by exciting the GQD sample by a series of excitation wavelengths (λ_{ex}) from 300 to 350 nm as shown in Figure 3-8(c). The PL response for less than 300 nm excitation wavelengths is very low compared to that for 350 nm > λ_{ex} > 300 nm. The PL emission was recorded in form of twin peaks at 442 nm (blue), and 493 nm (cyan) which steadily increased in PL intensity with λ_{ex} without shift. For most values of λ_{ex}, the intensity of 442 nm peak is less than that of 493 nm PL emission peak except for 310 – 330 nm excitation wavelengths. The GQDs excited at 350 nm showed most intense photoluminescence. All as-prepared GQD samples were pale yellow under ambient light and showed blue luminescence when illuminated by a 365 nm UV as photographed in Figure 3-8(d). The same sample when heated at 60 C for 3 hours on hot plate, changed its colour from pale yellow to a golden yellow and showed cyan instead of blue luminescence when exposed to a 365 nm UV lamp, due to agglomeration of the quantum particles. The approach presented here is scalable, offers a high yield of ~7 mg/ml and low cost synthesis of GQDs of desired size. The study also describes the significance and compatibility of the approach for solution process technologies to integrate the as synthesized GQDs in printed electronic devices, without addition of new solvents that may harm quality of GQDs. Here the solution processible GQDs embedded polymer thin films have been printed using electrohydrodynamic atomization (EHDA)[105] and employed in all printed flexible array of resistive switching devices. The successful integration of the approach with solution processible printing can assist future development of other GQDs based, thin film electronic and optoelectronic devices.

3.1.4 Synthesis of Graphene PVP Nanocomposite

PVP ink was synthesized by using previously reported ink synthesis methodology[163]. The viscosity of the ink was measured to be 27.7 mPa using a VM-10A viscometer. The graphene flakes were dispersed in 4 ml NMP solvent, bath sonicated for 30 min at room temperature and centrifugation was performed for 30 min at 3000 rpm. [183] The supernatant was collected from the graphene flake dispersion. For the synthesis of PVP/graphene blended dispersion, same weight percentage of PVP powder as used to synthesize the PVP ink was added to this graphene supernatant. The viscosity of this blended dispersion was measured to be 22.5 mPa.

3.1.5 Synthesis of Graphene Nanoflake/PVP Nanocomposite

PVP powder (10% wt.) and poly (melamine-co-formaldehyde 2%) as cross-linker were added to the filtered graphene nanoflakes in NMP. The mixture was then thoroughly mixed by employing bath sonication for 30 min, probe sonication for 10 min and magnetic stirring for further 24 hours. All steps were carried out at room temperature. The viscosity of the graphene/PVP nanocomposite in NMP was measured to be 19.5 mPa using a VM-10A viscometer.

3.1.6 Synthesis of Precursor for GQD/PVP Nanocomposite Memristor

A small quantity of Poly 4-Vinyl Phenol (PVP) in ratio 2:1 with GQDs was added to the GQD dispersion in NMP/DCB to synthesize the solution processible GQD/PVP nanocomposite. For uniform dispersion of PVP:GQD, bath sonication was used for 10 min and ultrasonication for 5 min.

3.2 Resistive switching in Graphene nanostructure composites

Various memristive devices were fabricated to explore their respective resistive switching characteristics. The active layers were realized by suitable composites of polymer with either Graphene flakes, Graphene Nanoflakes or GQDs.

3.2.1 RS in Graphene flake PVP composites

For the first polymer composite, Graphene flakes were used with polymer PVP. In this case three approaches were used whereby each memristive device was fabricated in ITO/active layer/Ag MIM sandwich structure as shown in Figure 3-9.

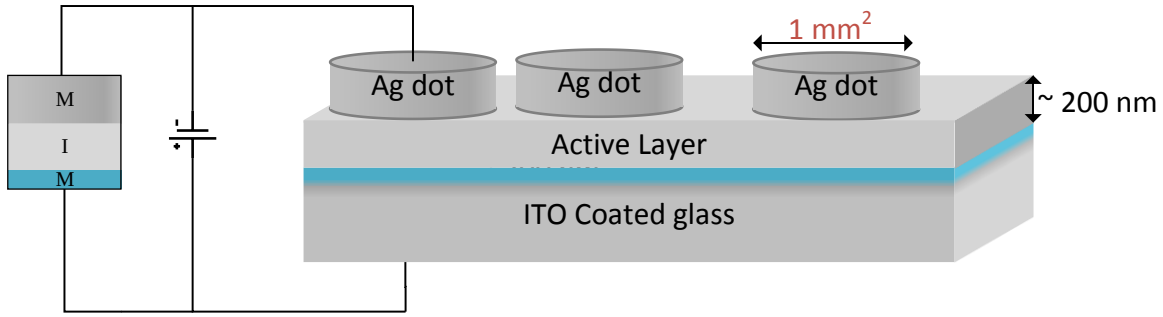

Figure 3-9: Schematic showing MIM structure for memristive device with the block diagram. The silver dot acts as top electrode whereas ITO acts as bottom electrode for sandwiched MIM memristive device.

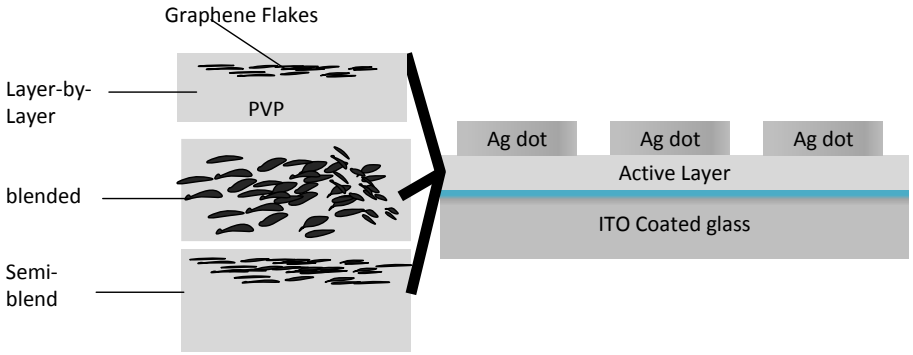

Figure 3-10: Schematic showing active layer within devices fabricated with LBL, SB, and blended approaches.

The active layers of devices have been summarized in Figure 3-10, differentiating the effect of three approaches on active layer formation. The schematic shown in Figure 3-11 summarizes the active layer fabrication process for the three approaches. In the first approach called layer-by-

layer (LBL) approach, PVP was spin coated on ITO coated glass at 1500 rpm and annealed at 100 ℃ for 1 h. Afterwards graphene dispersion was spin coated at 1500 rpm over the annealed PVP film and annealed at 100 °C for 6 h. For the semi-blend (SB) approach PVP film was spin coated on ITO coated glass and graphene dispersion was spin coated on it without annealing the PVP film.

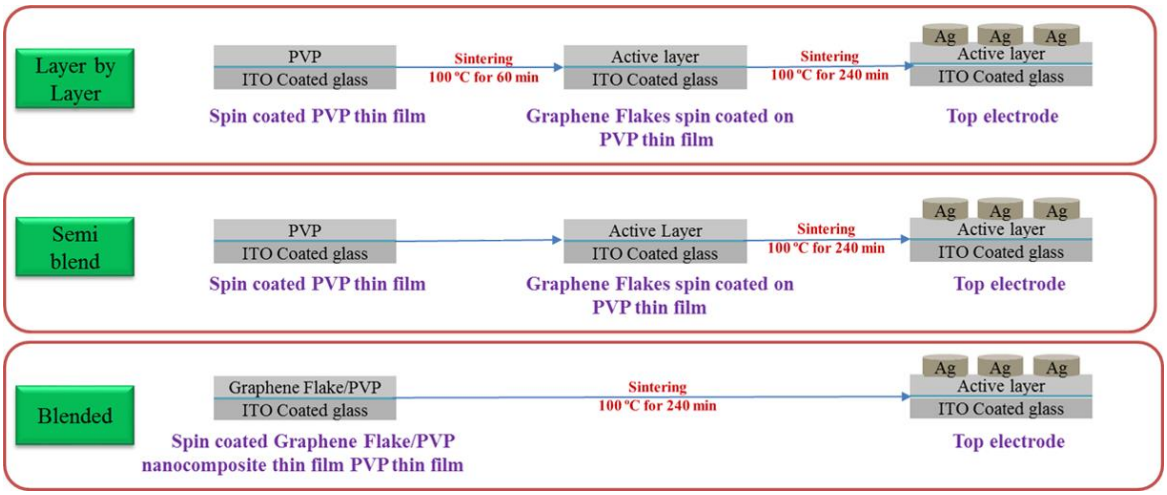

Figure 3-11: Spin coating the thin films of graphene and PVP using (a) LBL, (b) SB, and (c) blended approaches on ITO coated glass. The top electrode in each case is a silver dot less than 1 mm^2 diameter.

The films were annealed at 100 °C for 6 h after spin coating the two materials. The temperature was kept at 100 ℃ to safeguard the PVP film integrity. Blended PVP-graphene composite film was fabricated by spin coating PVP/graphene flakes dispersion on ITO coated glass substrate at 1500 rpm. The film was then annealed at 100 °C for 6 h. The LBL approach rendered a definite interface between PVP and graphene film on top of the PVP film. The films fabricated by SB approach lacks such structure because graphene flakes intrude the PVP near the interface. This decreases the individual thickness of the pure PVP and graphene films and PVP-graphene composite was formed at the interface between the two layers.

For each of these devices a dot of high conductivity silver paste of average area of less than 1 mm^2 was used as top electrode while ITO served as bottom electrode to complete MIM

memristive device. The double voltage sweep was applied across the two electrodes to study current-voltage characteristics of the devices.

3.2.1.1 Morphological analysis

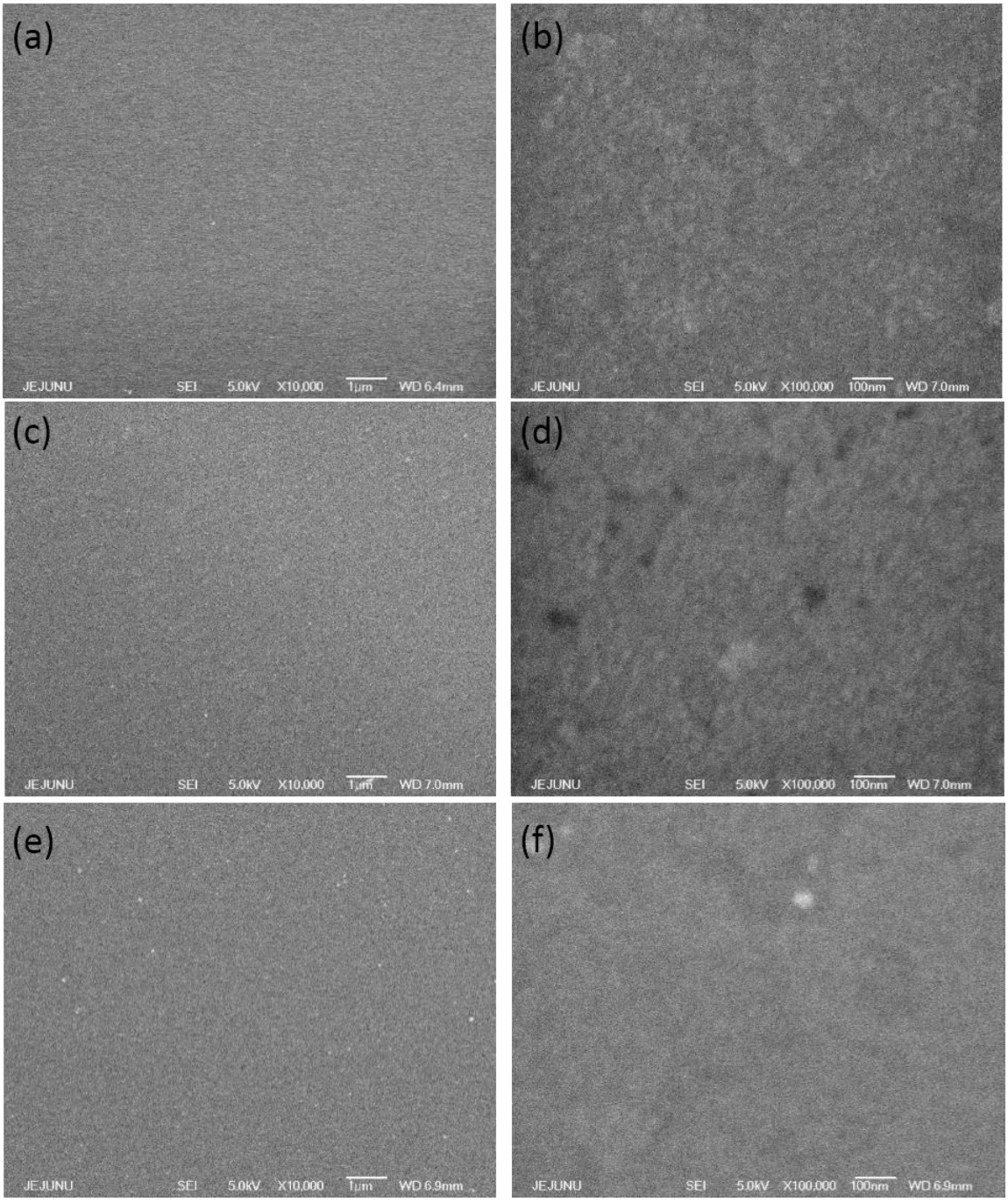

Figure 3-12: SEM images at low and high magnifications showing uniform surface characteristics for devices fabricated with LBL (a, b), SB (c, d), and blended (e, f) approaches.

Film thickness was measured by a non-destructive, thin film-thickness machine, K-MAC ST4000-DLX, based on interference spectrum of white light incident on the film surface. For each film, the thickness measurement was averaged after taking at least seven readings at different locations in such a way that the measurement represents almost all the area of sample. The results reveal that the active layers fabricated by LBL, SB and blended approaches were of good uniformity with average thicknesses of ~210±16, ~200±13, and ~170±11 nm, respectively.

The surface morphology plays a crucial role in performance of thin film devices. SEM analysis was performed for films fabricated by each approach (Figure 3-12). The films fabricated by LBL approach (a, b), SB approach (c, d), and blended approach (e, f) showed no cracks across films' surfaces and appreciably uniform surface morphology.

3.2.1.2 Electrical characterization

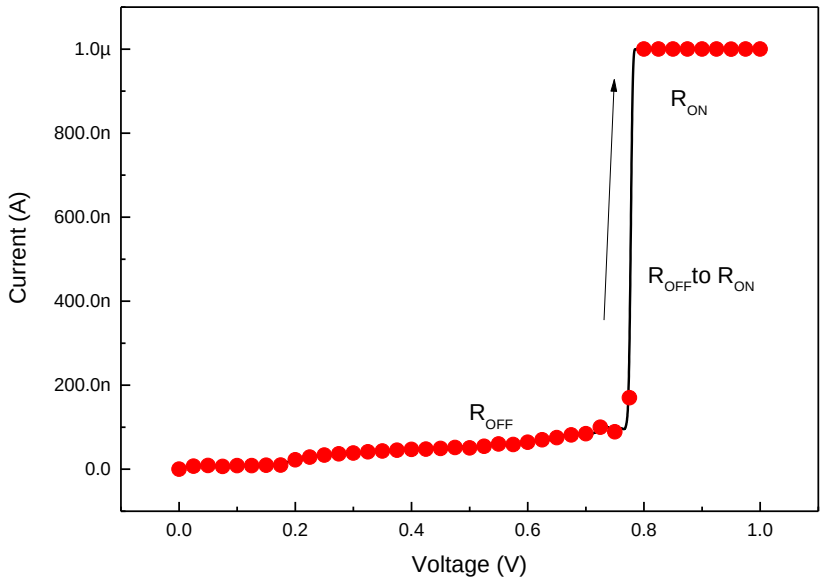

Figure 3-13: Forming of active layer occurred at just below 0.8 V at low compliance current of 1 µA. The resistance of the film drops and device is said be turned on from low current off state. The resistance has stepped down from R_{OFF} to R_{ON}

For the electrical characterization, I–V characteristics of the ITO/active material/Ag device were analysed by using the top Ag electrode connected to the driving voltage whereas keeping bottom ITO electrode grounded. The characterization was performed by initially applying a forming voltage, which is necessary for stable resistive switching operation [82,184,102]. The

electroforming process was performed by varying applied voltage from 0 to 2 V with compliance current (CC) of 1 µA on one of the devices as shown in Figure 3-13.

Three sets of identical devices were fabricated using each approach. The conventional I-V characteristics at 100 µA CC for 20 double voltage sweeps applied from +2 to -2 V are shown in Figure 3-14.

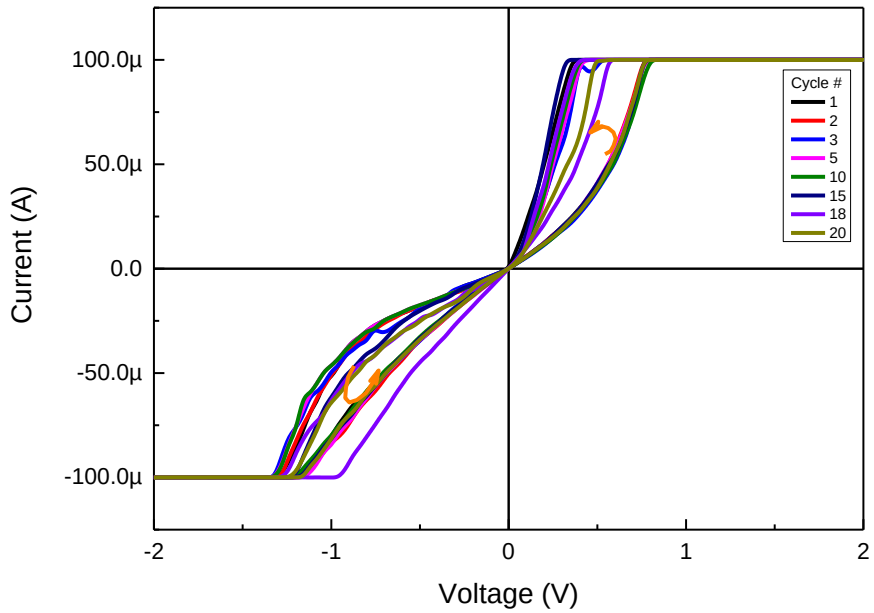

Figure 3-14: I-V characteristics of devices fabricated by blended approach. The memristive device characterized at compliance current of 100 µA. The devices fabricated by this approach were more robust as evident by number of voltage sweeps in legend

The blended layer devices performed appreciably showing stable switching during voltage sweeps. The voltage was first increased from 0 to 2 V keeping 100 µA CC to avoid hard breakdown of devices due to overflow of current. The low current allowed by the device was termed as the HRS for the device. Upon decreasing the voltage back from 2 to 0 V, the current did not decrease but device allowed more current to flow through it. This state was defined as the LRS since it showed lower resistance to the flow of current as shown by the changed slope of I-V curve when voltage was decreasing from 2V to 0V. This state transition can be clearly seen to have occurred at 0.8 V. When the voltage was gradually decreased from 0 to -2 V, Schottky behaviour became prominent, the current reached and remained constrained to 100 µA beyond -1.2 V. The voltage was then changed from -2 to 0 V gradually but this time the device switched from this HRS to LRS at around -0.9 V again, thereby completing the pinched hysteresis loop. During voltage sweep

between -2 and 2 V, the I-V plot was not symmetric across 0 V line. However, repeated voltage sweeps, show both the retentivity and stability of the blended layer device are better than the devices fabricated by other two approaches. The blended layer devices sustained more than 20 double voltage sweeps whereas the other devices were not able to sustain the repeated voltage sweeps. Figure 3-15(a) shows the semi log I-V characteristics of blended memristive device at 100 µA CC, each voltage sweep carried out at 60 s interval between voltages of 2 and -2 V. The endurance of the fabricated device was tested by applying multiple voltage sweeps. Figure 3-15 (b) shows the endurance analysis of the fabricated device at a reading voltage (V_{READ}) of around 0.4 V. Figure 3-15 (b) shows a consistent OFF/ON ratio of more than 5.

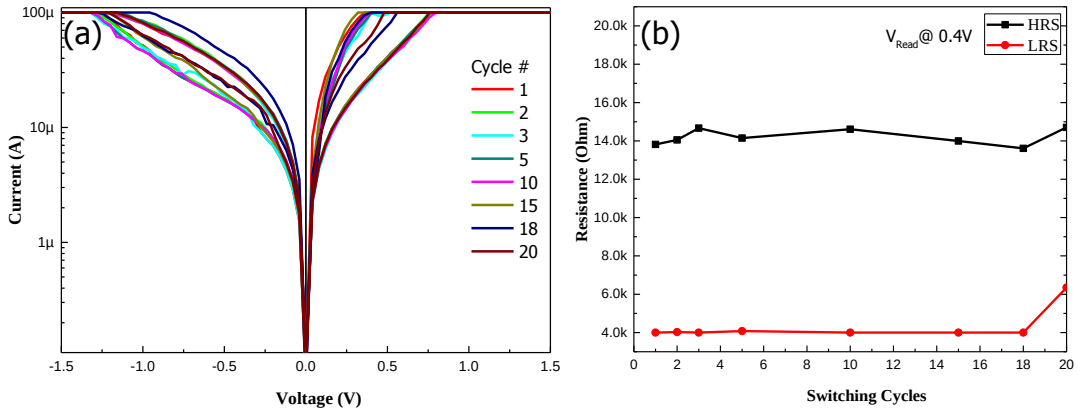

Figure 3-15: (a) Semilog I-V characteristics of blended memristive device at 100 µA CC, each voltage sweep carried out at 60 s interval between 2 and -2 V. (b) Resistance vs switching-cycle graph indicating ON/OFF ratio of roughly 5:1. The reading voltage was around 0.4 V for the measurements. The device performed appreciably up to 20 voltage sweeps.

The average resistance during the OFF state remained about 14 kΩ and decreased to about 4 kΩ during the ON state. Resistance variation of the HRS and LRS for the same device was evaluated. R_{OFF}/R_{ON} was observed to be approximately 5 when read at V_{READ}=0.4 V. The IV characteristics for devices fabricated using each blended, LBL and Semi blend approaches at 5

mA CC are shown in Figure 3-16.

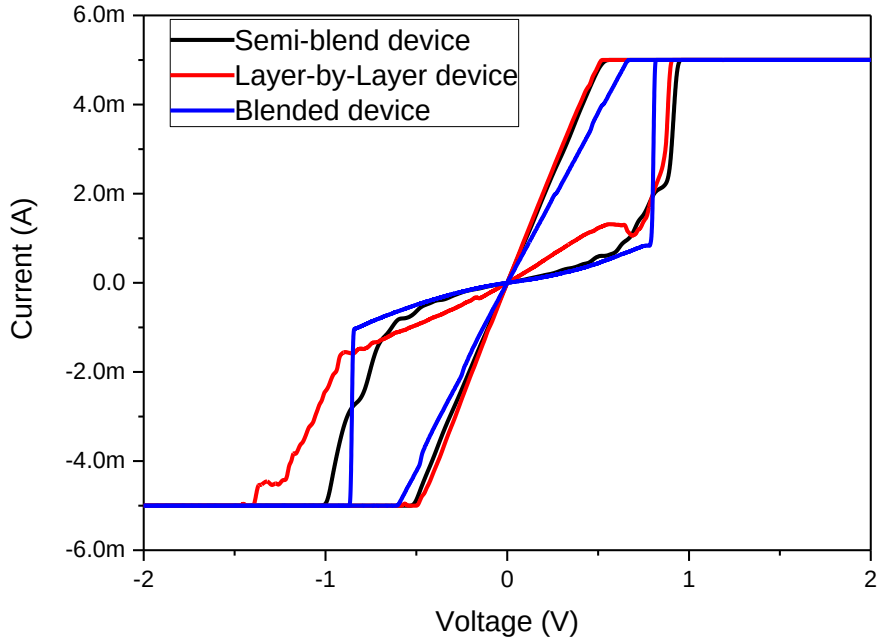

Figure 3-16: First double voltage I-V sweep for the devices at 5 mA CC fabricated by blended, SB, and LBL approaches. Most devices fabricated by SB and LBL approaches did not withstand 10 voltage sweeps, and the memristive behavior was unstable after 10th voltage sweep. Only blended device was able to retain switching characteristics for more than 20 voltage sweeps without failing.

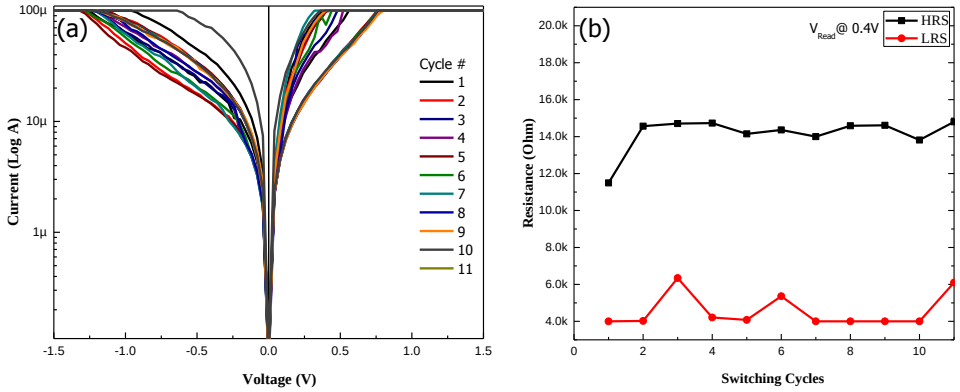

Figure 3-17: (a) Semilog I-V characteristics of LBL memristive device at 100 µA CC, each voltage sweep carried out at 60 s interval between 2 and -2 V.(b) Resistance vs switching-cycle graph indicating ON/OFF ratio for the LBL fabricated device.

The devices in each of these cases showed memristive behavior initially for first few voltage sweeps. However, only the blended devices were able to withstand and retain switching behavior for more than 20 voltage sweeps. The LBL and semi blend devices could not repeat the switching behavior beyond 10 voltage sweeps. Figure 3-17 shows semi-log I-V characteristic for 10 double voltage sweeps performed at 100 µA CC.

The endurance test on this type of device in Figure 3-17 shows that the device's HRS and LRS values were not uniform but changed during first 10 cycles. For a batch of 3 devices tested for each approach, no LBL device withstood more than 11 voltage sweeps even at 100 µA CC.

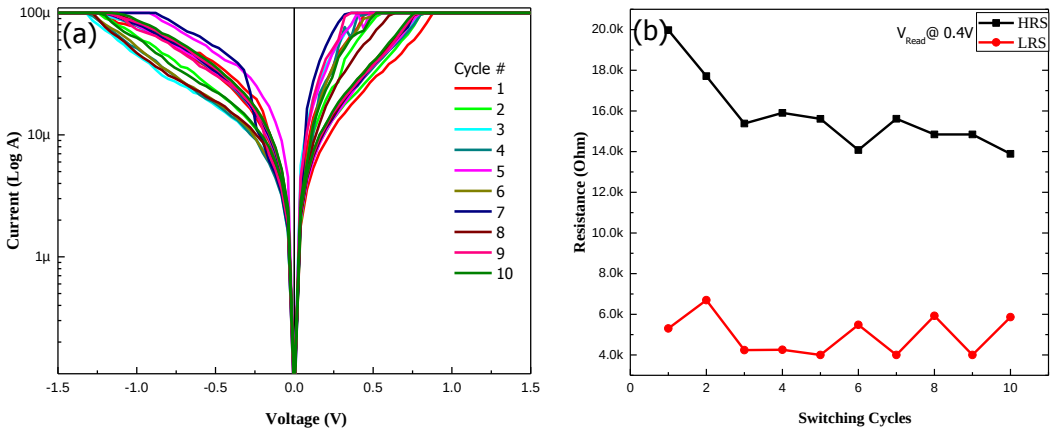

Figure 3-18) (a) Semilog I-V characteristics of SB memristive device at 100 µA CC, each voltage sweep carried out at 60 s interval between 2 and -2 V. (b) Resistance vs switching-cycle graph indicating ON/OFF ratio was lower and non-uniform compared to blended device. The reading voltage was around 0.4 V for the measurements

The device fabricated by SB approach showed even worse endurance and unstable resistive switching as shown in Figure 3-18.

The device initially showed a high HRS of about 20 kΩ, which kept decreasing until the device got hard breakdown. SB memristive devices had an unstable LRS which varied between 6 to 4 kΩ. The R_{OFF}/ R_{ON} for LBL and SB devices were calculated to be just above 3 at 100 µA CC for same time and voltages as done for blended active layer based devices.

The blended approach yielded most stable memristive behavior among the three approaches. The performance of the memristive devices based on SB and LBL approaches lacked stability at 5 mA CC. The reason for better memristive behavior in blended device is proposed to be due to the formation of composite structure and thus improvement in uniformity within the active layer. The graphene flakes get embedded within the PVP polymer matrix and thus enhance the charge

trap densities within the device active layer. Since the memristance behavior is enhanced for thinner insulating films, this factor can be attributed as the reason for comparatively stable performance of the blended structure memristive device. Considering I-V characterizations, the blended approach showed better memristive behavior compared to SB and LBL approaches. The graphene flakes in case of LBL approach were not embedded within the PVP polymer matrix but formed a conducting layer on top of the highly insulating PVP films. The cross section of films fabricated by SB approach had three different. The top part of conducting graphene flakes, the bottom part of PVP only while the middle one becomes a PVP-graphene composite. The memristive behavior scales with the insulating layer thickness. The device based on SB approach showed unstable and low endurance memristive behavior due to lack of uniformity and variation of materials across the two electrodes. This non-repeatability was due to formation of simultaneous multiple conducting filaments within the active layer. The graphene oxide memristor fabricated by EHDA [102] technique also reported similar ON/OFF ratio.

3.2.2 Graphene/PVP nanocomposite based flexible memristor

3.2.2.1 Device fabrication

The conjet and atomization of Graphene nanoflake/PVP nanocomposite ink has already been explain as introduction to EHDA section. The deposited thin films were sandwiched between ITO and Ag top electrode. A small dot of high conductivity Ag paste, of an average area ~1 to 3 mm^2 was used as top electrode for all devices. Whereas ITO served as bottom electrode to complete MIM memristive device. Double voltage sweeps were applied across the two electrodes, to study current-voltage characteristics of the devices.

3.2.2.2 Morphological analyses

For each thin film used as an active layer, the thickness was measured by taking average of at least 7 measurements at different locations of film, repeated one after the other, in such a way that the set of measurements represented almost the whole top surface of the sample. The results reveal that the active layers fabricated by EHDA show good uniformity with average thicknesses of ~140 ±7 nm.

Surface morphology of printed nanocomposite film on ITO coated PET substrate were analysed using 3D Nanomap surface analyser and FESEM. The surface profiler with nanoscale accuracy was used for surface roughness measurement in phase shifting interferometry (PSI) mode. The 2D, X-direction, and 3D surface profiles of graphene/PVP nanocomposite thin film have been shown in Figure 3-19(a) to (c) respectively. The average roughness observed for the film is 2.59 nm, while the film linear variation in roughness along x axis is about 9.47 nm. Figure 3-19 (d) and (e) show low and high resolution FESEM images of deposited graphene/PVP nanocomposite respectively. Thus FESEM images reveal uniformity of films, devoid of cracks, voids or humps at nano-scale. This attribute plays important role for reliable working of thin film, employed in electronic devices. The inset in Figure 3-19(e) shows the FIB image of the nanocomposite thin film deposited on top of ITO coated PET substrate. The observed thickness of the thin film was about 150 nm in close agreement with thickness profiler data. The Pt coating was deposited to protect the film from possible damage during sample preparation.

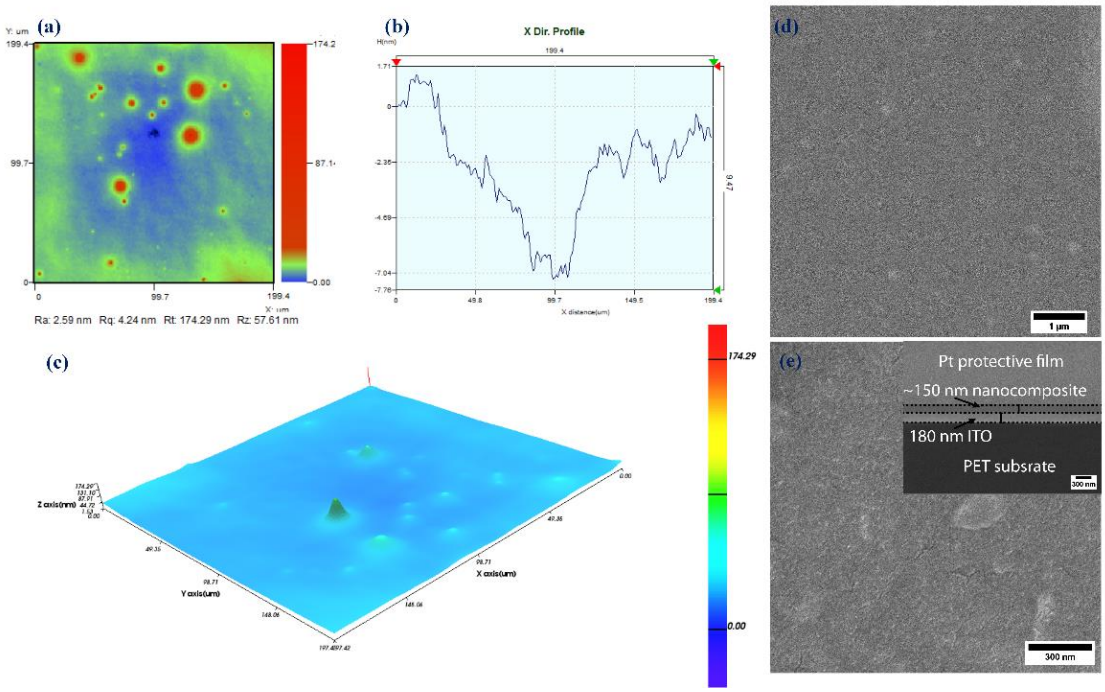

Figure 3-19: Morphological analysis of thin film using 3D Nanomap for (a) two-dimensional map film roughness, (b) linear roughness plot along x-axis, and (c) three-dimensional map for the film surface shows the occasional protrusion of graphene flakes in PVP thin film. (d) Low magnification scale bar =1 µm (e) high magnification scale bar =300 nm SEM micrographs also show uniformly deposited composite thin films by EHDA. The Inset shows the FIB cross sectional image of the nanocomposite film deposited on top of ITO coated PET substrate

3.2.2.3 Optical characterization

The optical transmittance of thin films collected by UV/VIS/NIR Spectrophotometer, shows that the composite thin films were optically transparent in visible and near infra-red region (NIR), showing promise for use in optoelectronic applications as shown in Figure 3-20. The composite film showed negligible transmittance in UV region below 288 nm, and a sharp increase in transmittance with gradual increase in incident wavelength from 288 to 377 nm. The transmittance remained about ~87 % beyond 377 nm in visible and NIR regions. FT-IR analysis [Bruker 66/S, Germany] for functional groups in graphene nanoflakes after ultra-sonication has been shown in Figure 3-21. The peak at ~3436 cm^{-1} is attributed to –OH, whereas 2926 and 2852 cm^{-1} represent the C-H stretch vibrations [185]. The absence of characteristic graphene oxide peaks shows that the processing in presence of NMP does not induce any oxidation in graphene flakes. NMP assisted exfoliation and break down of the graphene flakes into even smaller parts has been evidently

shown in TEM images

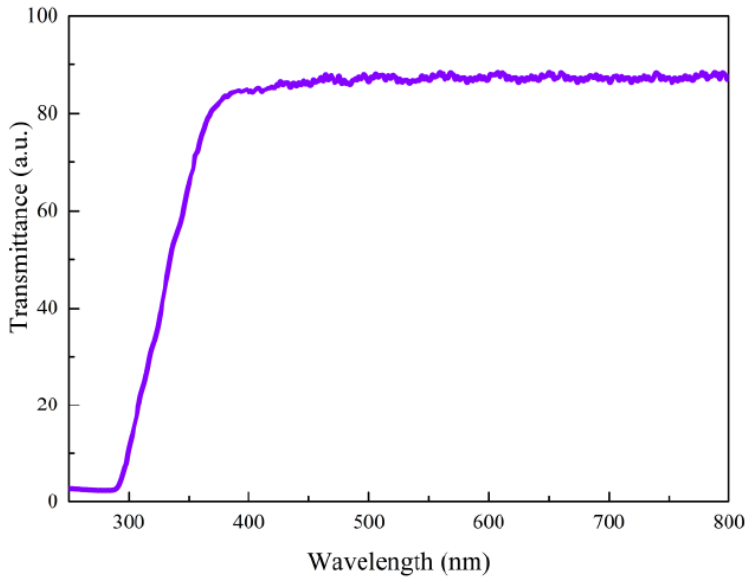

Figure 3-20: Transmittance spectrum of composite film shows up to 87% transmittance in visible and near-infrared regions. The films show strong absorbance in ultraviolet region.

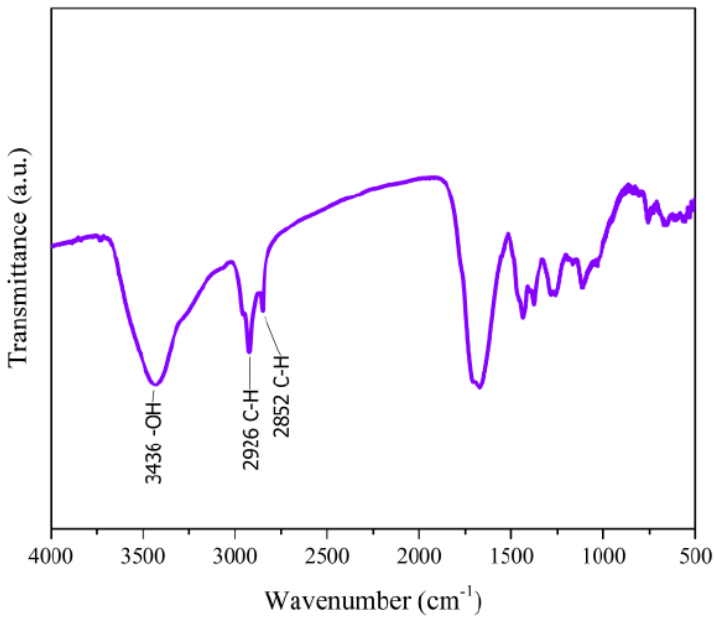

Figure 3-21: FTIR spectrum of graphene nanoflakes after processing by stirring, shaking and ultra-sonication.

3.2.2.4 Electrical characterization

The electrical properties of the fabricated Ag/organic nanocomposite/ITO device were further analysed by resistive switching studies. For current–voltage (I–V) characteristics the ITO/active material/Ag device was biased by connecting Ag, the top electrode to driving voltage whereas ITO, the bottom electrode was grounded. The characterization was performed by initially applying a forming voltage, which is necessary for stable resistive switching operation [82,184,102] as shown in Figure 3-22. The electroforming process was performed by varying applied voltage from 0 V to 7 V, with compliance current (CC) of 100 µA. Initially device started in HRS and switched to LRS after a voltage of about 3V.

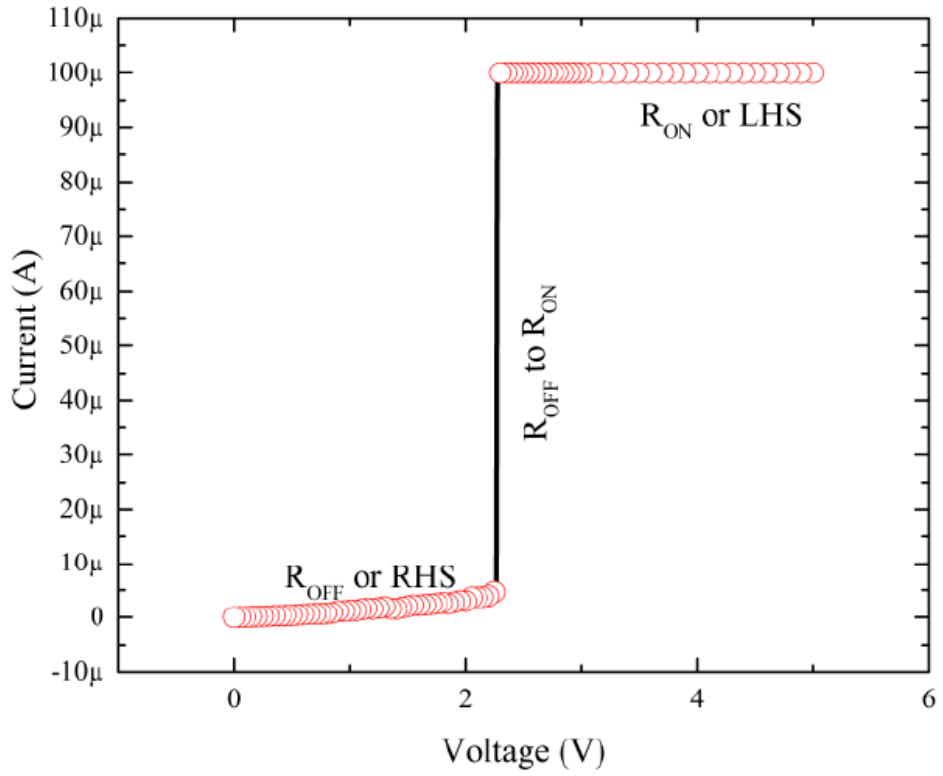

Figure 3-22: Electroforming of Graphene/PVP nanocomposite film as memristor performed by slowly increasing potential across composite film as an active layer in Ag/active layer/ITO memristor device

After performing the electroforming process, double voltage sweeps between extremes of -3 and +3V were used to analyse the resistive switching behaviour of device. The magnitude of applied voltage is fairly small compared to other printed electronic devices[186]. The voltage sweeps was applied repeatedly to evaluate memristor behaviour at low compliance currents (CC) of 10

nA. The conventional Semilog I-V characteristics at 10 nA CC, for one of the double voltage sweeps applied between -3 and +3V is shown in Figure 3-23.

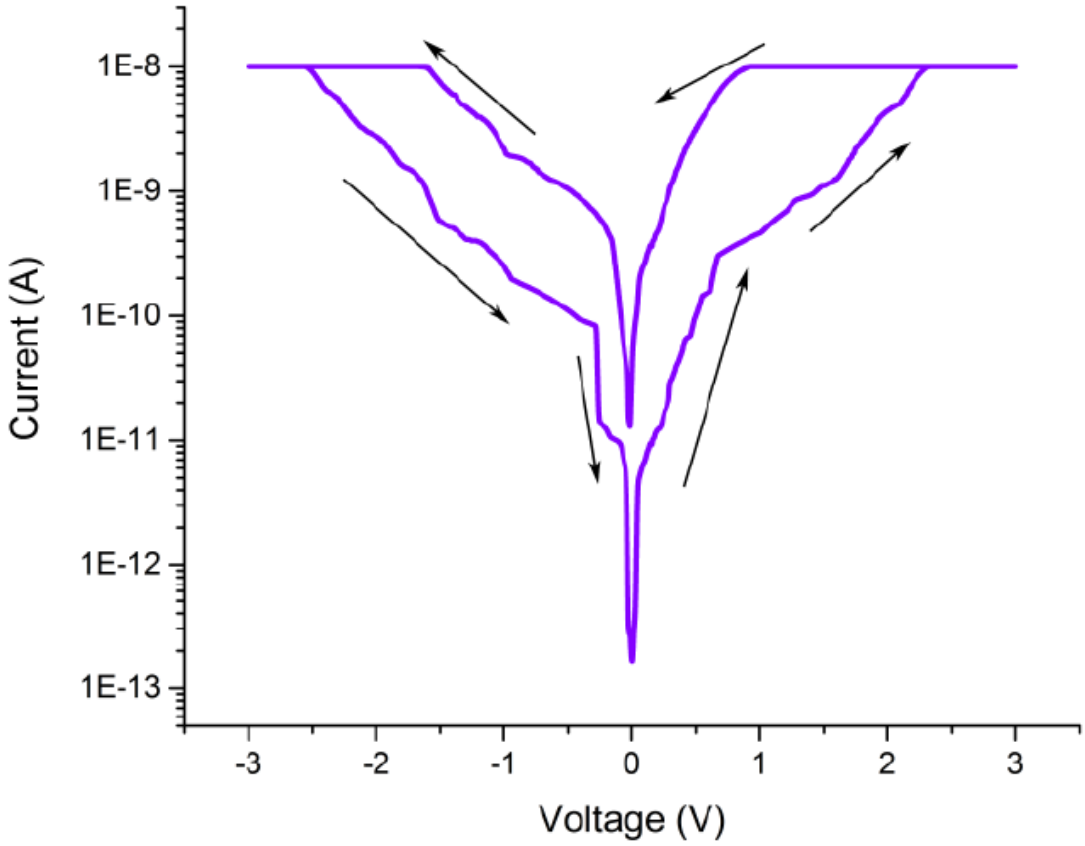

Figure 3-23: Semilog I-V characteristic of Nanocomposite film used as a memristor at 10 nA compliance current

The devices exhibited remarkable stable resistive switching behaviour, by sustaining the resistive states, for repeated voltage sweeps. Figure 3-24 shows the device robustness for resistive states in the device, on application of multiple voltage sweeps. The voltage was first increased from 0 V to 3 V keeping 10 nA CC to avoid hard breakdown of devices due to overflow of current. The low current allowed by the device was termed as the HRS for the device. The device switched to high current state, called LRS after about 2V. However, decreasing the voltage from 3 to 0 V, the current did not decrease as the high current continued to flow through the device, until about 0.8 V, after which the current started to decrease and reached zero at 0 V. This state was defined as the LRS, since it showed lower resistance to the flow of current as shown by the changed slope

of I-V curve when voltage was decreasing from 3 V to 0 V. This state transition can be clearly seen to have occurred at 0.8 V.

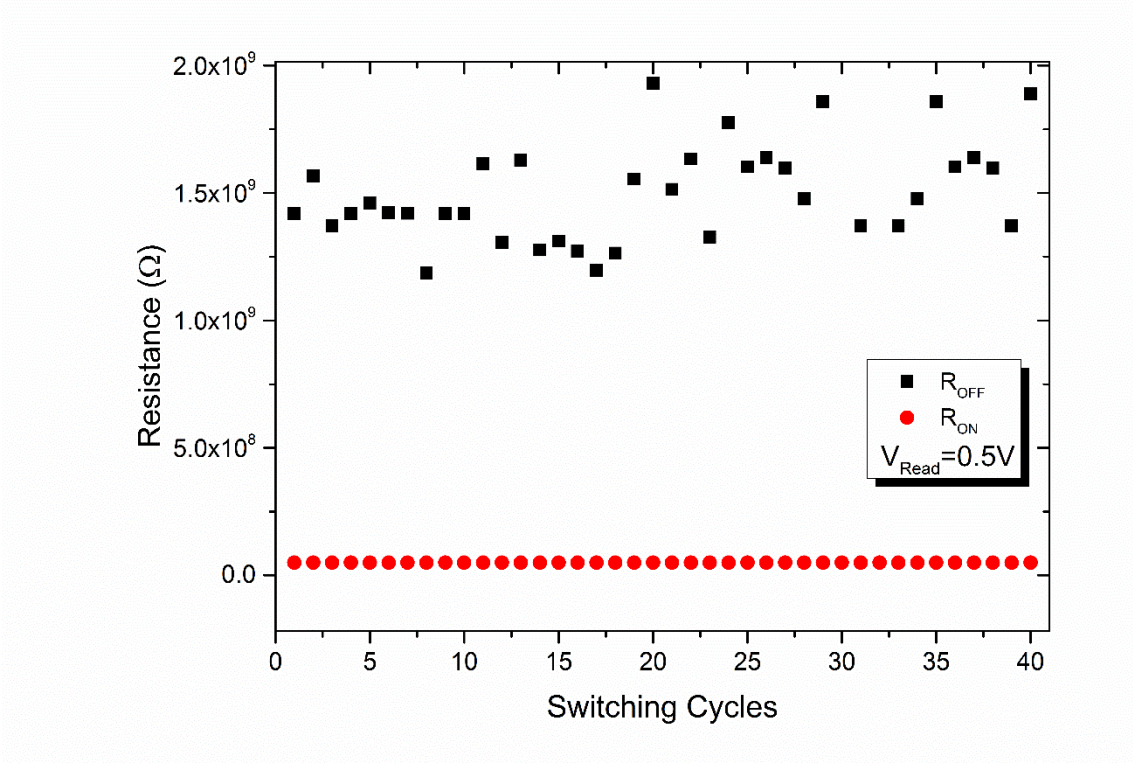

Figure 3-24: The endurance test performed by applying multiple voltage sweeps between -3 and 3 V at VREAD =0.5V

When the voltage was gradually decreased from 0 to −3V, Schottky behaviour became prominent, the current reached and remained constrained to 10 nA beyond −1.2 V. Changing applied voltage from -3 to 0 V, device showed change in resistance state at about -2.5 V and finally showed 0 A at 0 V, hence completing the characteristic hysteresis loop.

The devices showed stable memristive behaviour due to the Ag conducting filament formation and rupture within PVP matrix. However the resistive switching is further stabilized due to charge trapping within highly conductive nanographene in composite thin film[169,187,188]. The graphene nanoflakes embedded within the PVP polymer matrix, enhance the charge trap densities within the device active layer. Since the memristance behaviour is enhanced for thinner insulating films, this factor can be attributed as the reason for stable performance of the Graphene/PVP nanocomposite memristive device. More than 80% devices in our current study, with sandwiched composite films used as resistive switching devices showed consistent switching behaviour for

endurance testing, retention time, and flexibility. The Values of LRS and HRS were appreciably stable. The average value of HRS read at 0.5 V was about $1.55 \times 10^9 \Omega$ and $5 \times 10^7 \Omega$ for the LRS after 40 consecutive voltage sweeps between -3 and +3 V. The average R_{OFF}: R_{ON} remained consistently around 35:1, which is vital for a memory device. The retention time of the fabricated memristor was measured to be over 1 hour as indicated in Figure 3-25 and are expected to retain the resistive states for longer periods as well.

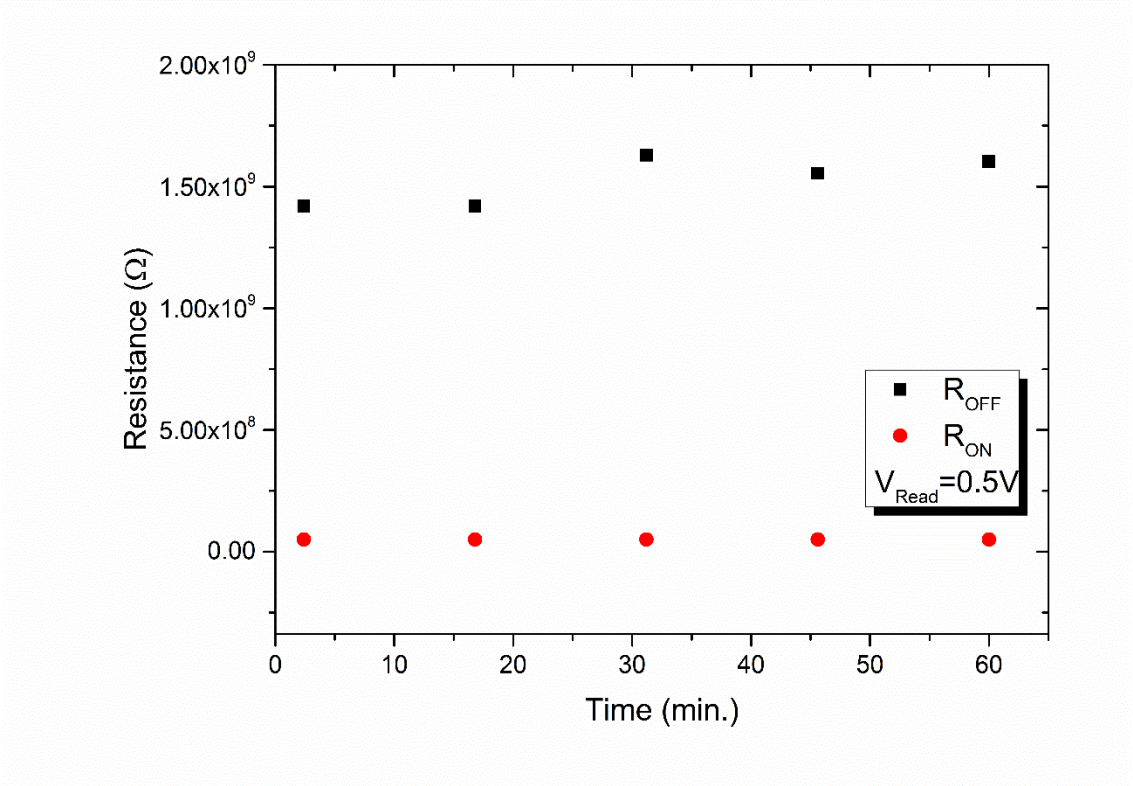

Figure 3-25: Device retentivity of over 1 hour measured for the Graphene/PVP composite memristor measured at 0.5 V.

PET has served as a good substrate for fabricating flexible electronic devices. The device's ability to retain its function when flexed, shows its feasibility for flexible electronics applications. The flexibility of the devices fabricated on PET substrates was examined by flexing devices from flat Figure 3-26(a) to a semi-circle Figure 3-26 (b) repeatedly for at least 50 flexes by wrapping them around cylindrical rods Figure 3-26(c). The slight variation in the HRS and LRS of device when bent to various diameters from 3.5 cm to 1.5 cm, Figure 3-26(d) shows flexibility of the device at varied bending radii.

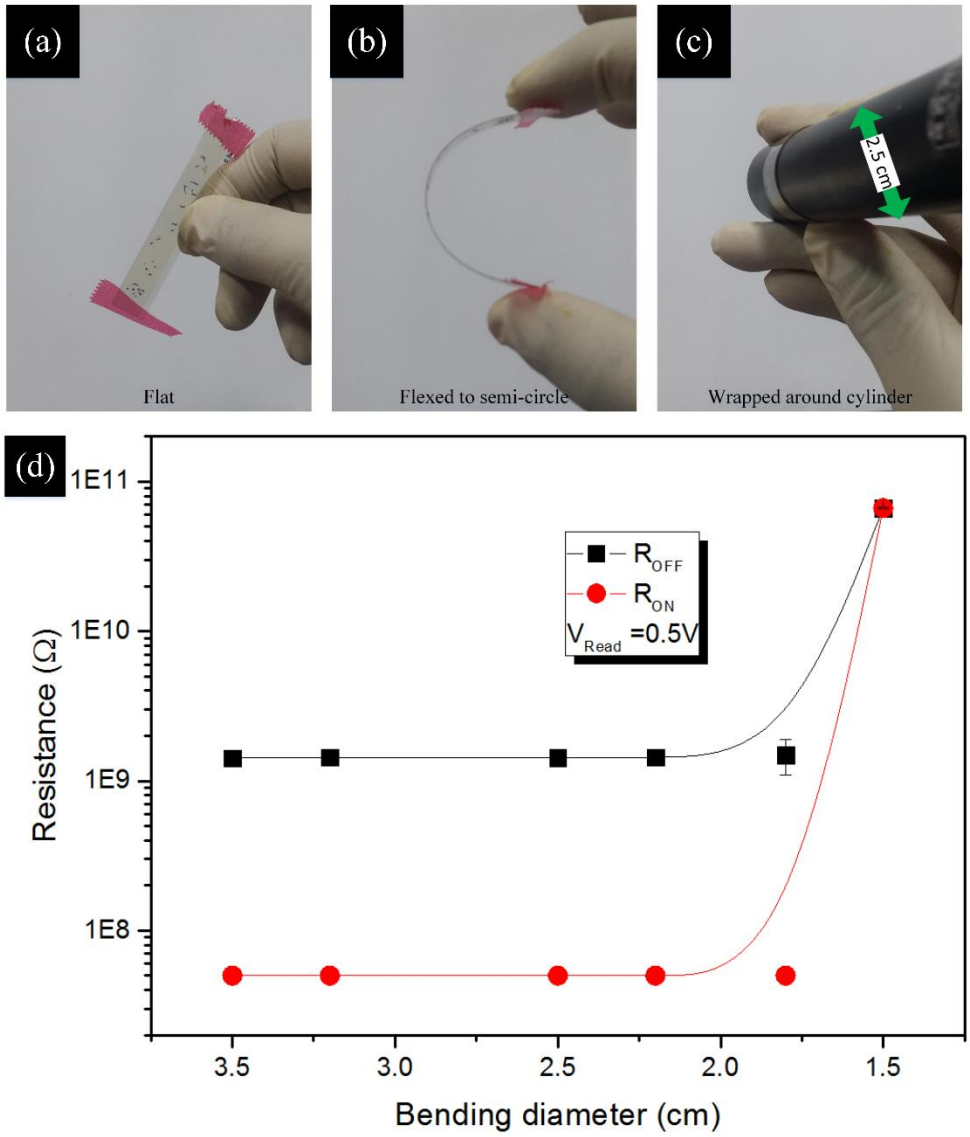

Figure 3-26: Evaluation of flexibility of the fabricated device. The devices are flexed between (a) flat to (b) a semi-circle for 50 continuous flexes by wrapping around cylinders of different diameters. (c)Devices wrapped around a cylinder with 2.5 cm diameter. (d) The variation in device's states when wrapped around cylinders of various diameters from 3.5 cm to a minimum of 1.5 cm

The devices bent beyond 1.8 cm, became open circuit due to silver electrode cracking and breakdown. This limit could be lowered further for even shorter bending radii if top electrode had been more flexible. Stable HRS and LRS in these devices, show their potential for flexible resistive switching applications.

3.2.3 All printed Poly(4-vinylphenol)–graphene quantum dot based memristor

The solution processible GQDs based nanocomposite with PVP was used for fabrication of PVP/GQD thin film memristor. For the fabrication of a flexible GQD–polymer nanocomposite memory device, mass printing technologies, such as EHDA and roll to plate were employed. A 2x2 array of 4 resistive switching devices was fabricated with insulating polymer (PVP) used as host material for the GQDs. The top and cross section views of the device has been schematically shown in Figure 3-27(a). PET substrates were cleaned using ethyl alcohol, deionized water and the exposed to UV light for 5 minutes. The development of the patterned Ag top and bottom electrodes was carried out employing roll to plate technology. Here 11 kgF force waste applied for pattern transfer with a delay time of 3 sec. Fine ~250 μm wide Ag patterns were achieved after sintering the samples at 100 ℃ for 1 h as shown by optical microscope micrograph in Figure 3-27(b).

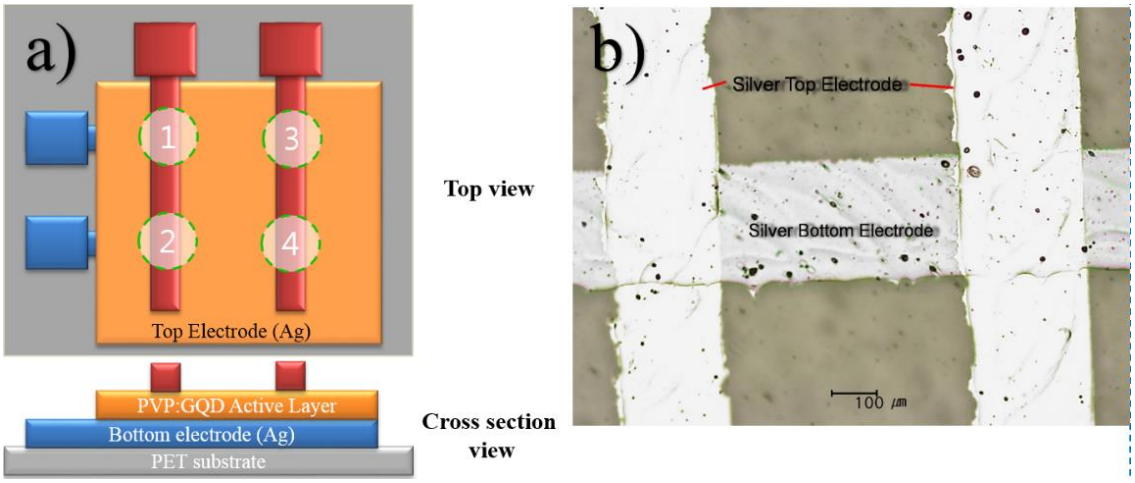

Figure 3-27: Schematic diagram all printed GQD based flexible resistive switching 2x2 array top view [top left] and cross section view [bottom left]. b) The optical microscope image showing the cross points of Ag electrodes sandwiching the solution processed transparent GQD embedded polymer active layer

Prior to deposition of active layer, part of Ag bottom electrodes as columns was carefully masked by tape for electrical connections. The thin film of nanocomposite as active material (~100 nm) was deposited using EHDA setup. After curing the deposited thin films at 100 ℃ for 2 h, rows of top electrodes were deposited on top of active layer again by roll to plate technology. The top and bottom electrodes crossed each other at 4 locations with active layer sandwiched between them, hence forming memristors. High Figure 3-28(a) and low Figure 3-28(b) resolution FESEM images of nanocomposite thin films evidently prove the uniformity of the thin film. The thickness

measurement was averaged after taking at least seven readings at different locations in such a way that the measurement represents almost all the area of thin film surface. The calculated thickness of thin film was 120±19 nm.

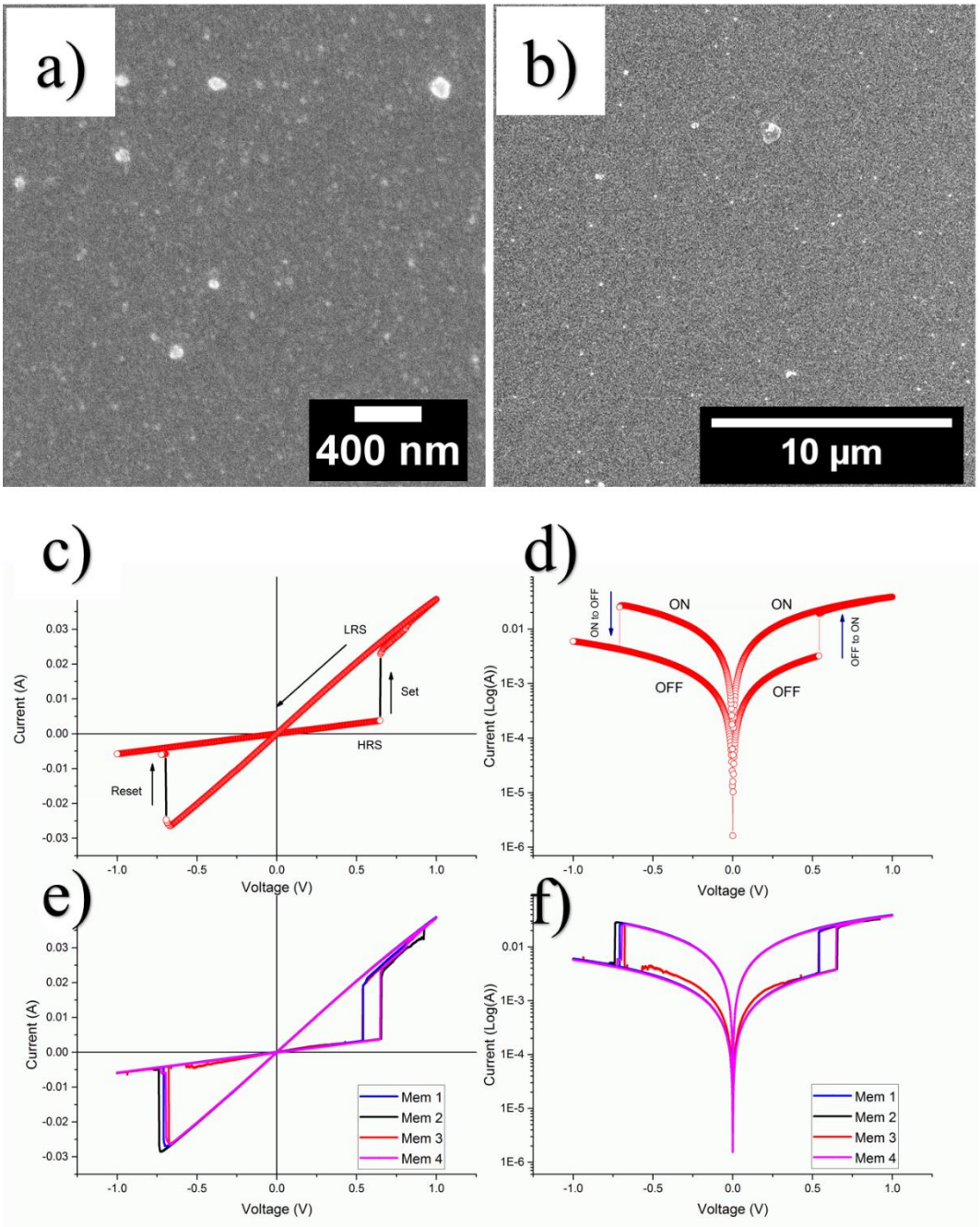

Figure 3-28: a) High resolution b) low resolution FESEM images. c) First I-V and d) Semilog I-V plots for a memristor. e) The comparison of I-V and f) Semilog characteristics of four memristors of the 2x2 memristor array

In order to study the electrical properties of the as-fabricated 2x2 array of 4 resistive switching devices, current–voltage (I–V) measurements were performed at room temperature by using a semiconductor characterization system. For each of the as-fabricated Ag/PVP: GQD/Ag memristor, the bottom Ag electrode was grounded whereas the bias was applied to the top Ag electrode. The voltage stress was applied on the highly resistive pristine device (>10^3 Ω), in a sequence of 0 V to +1 V to 0 V. By steady increase of the voltages imposed on individual device, a pronounced change of resistance from the pristine high resistance state (HRS) to the relative low resistance state (LRS) is observed at a SET voltage of about 0.65 V. After the transition from HRS (~170 Ω) to LRS (~28 Ω) the device remained in LRS, for the subsequent sweep from +1V to 0 V. The device shows no current when voltage drops to 0V. During steady voltage transition 0 V to -1 V to 0 V, the devices keep steady LRS state. The resistance steadily increases with increase in magnitude of negative voltage until it reaches RESET voltage, V_{max}= -0.69 V. Beyond V_{max}, the current decreases rapidly, switching device OFF to the HRS from LRS state as shown in Figure 3-28(c). Figure 3-28(d) elaborates the semi-log I-V response of the same memristor. Figure 36e and 36f compare the I-V and semi-log I-V responses for each of the four devices. The four devices show negligible change in memristor parameters. The robustness of the array was tested by applying voltage stress cycles on each of the four devices. The voltage stress applied on the devices showed stable switching for 100 repeated voltage stresses Figure 3-29(a) and retentivity of over a day as shown in Figure 3-29(b). The striking difference for the GQD embedded PVP based memristor with other PVP based memristors fabricated in past was the ability to withstand higher currents without breakdown, despite operating at more than 50 mA compliance currents. The very small variation in resistance states for memristor M1 dictates stability of the device over large number of voltage cycles as well as time and showed stability for over well 24 h. To evaluate flexibility of the PET based memristor array, it was flexed for over 200 times, yet the device remained undeterred for its memristor function as shown in Figure 3-29(c) whereas the devices had remarkable performance for repeated bending cycles. The minimum bending diameter of 1.5 cm was observed as stable limit for device to function without breakdown. The device broke down

when bent for diameter 1.2 cm as shown in Figure 3-29(d).

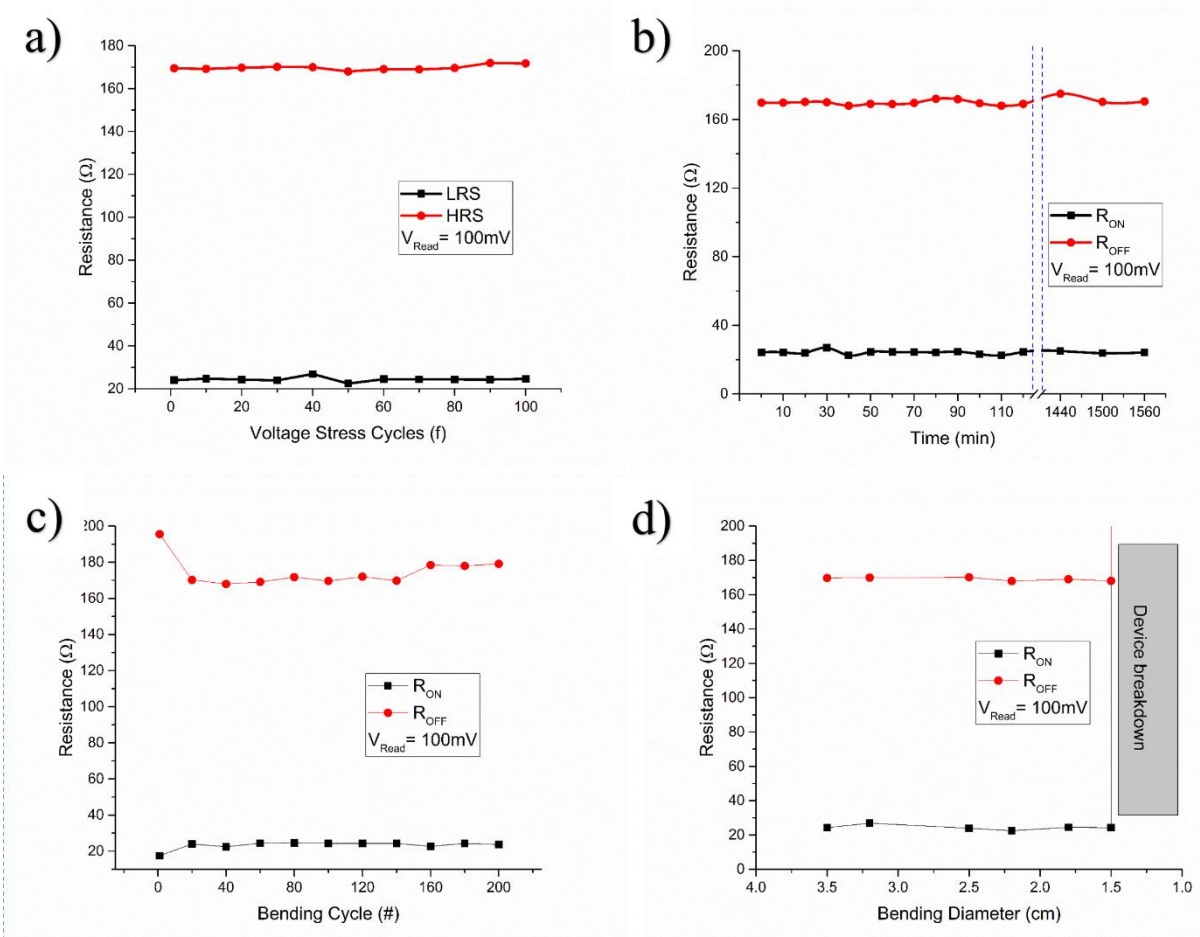

Figure 3-29: The resistive switching characteristics of the devices. a) The voltage stress cycles b) c) retentivity and d) flexibility tests performed for the memristors at V_{Read}= 100 mV

Chapter 4. CONCLUSIONS AND FUTURE WORK

4.1 Conclusions

The Synthesis mechanism used for fabrication of Graphene nanostructures has proven its utility for resistive switching devices and can be extended to other 2D materials such as MX_2. For synthesis of nanoflakes and even for quantum dots. The EHDA, roll to plate and screen printing technologies have proved their ability to print resistive switching devices and arrays that can be extended to roll to roll based mass printing. Although only 2x2 array of memristors has been reported here. The modified mesh and plate design can be used to extend the array to higher nxn matrix for multibit memory device. The GQD synthesis technique is compatible with solution based thin film printing systems, and good yield of 7 mg/ml. The GQDs showed strong absorption in UV and deep UV ~290 nm, and luminescence for 365 nm UV lamp, PL emission peaks were observed at 442 and 492 nm for laser excitation wavelengths varied from 300-350 nm. The peak intensities increased with increase in excitation wavelength. The GQD/PVP nanocomposite was successfully synthesized and EHD atomized on target substrate. All printed GQD/PVP nanocomposite memristors in the 3x3 array showed OFF/ON ratio ~10, retentivity of over 24 h, flexibility up to 1.8 cm for over 200 cycles and robustness to withstand more than 100 voltage stress cycles. Graphene nanoflake (20-200 nm) were synthesized from layer graphene flakes, diameter >1 µm by ultra-sonication, magnetic stirring and mechanical shaker, in presence of NMP. Nanoflake PVP nanocomposite ink formulation was adjusted for EHDA compatibility and EHD atomized on ITO coated PET Transmittance of Graphene nanoflake/PVP nanocomposite thin film was ~87%. SEM and surface profilometry showed uniform thin films. Nanocomposite films, sandwiched between Ag and ITO were studied for resistive switching at 10 nA. The devices showed an excellent OFF/ON ratio of 35:1, tested retentivity up to an hour, flexible enough to withstand 50 continuous bending cycles and showed robustness for at least 40 voltage stress cycles. A non-processed graphene composite deposited using three different approaches was also explored for resistive switching. Three approaches, layer by layer, Semi-blend and blended approaches were used to deposit graphene flakes (unprocessed, exfoliated in NMP) and PVP. Among the three approaches for active layers fabrication, the blended approach was better compared to semi blend and layer by layer approaches. The fabricated devices showed better robustness to multiple voltage sweeps at lower compliance current of 100µA compared to 5mA. The Roff/Ron for devices

fabricated by blended approach was 5 and consistent for more than 20 voltage stress cycles. However the presence of graphene flakes in this form did not enhance the memristive behavior of PVP.

4.2 Future work

The luminescent properties of Graphene quantum dots synthesized in the work presented here are worth further exploration for photonic devices such as photodetectors. The technique employed for synthesis of graphene quantum dots can be explored to other 2D materials for futuristic photonic and electronic devices. The effect of replacing PVP polymer in graphene PVP composite can also be explored to devise resistive switches with higher retentivity and better OFF to ON ratios.

REFERENCES

(1) Novoselov, K. S.; Geim, a K.; Morozov, S. V; Jiang, D.; Katsnelson, M. I.; Grigorieva, I. V; Dubonos, S. V; Firsov, a a. Two-Dimensional Gas of Massless Dirac Fermions in Graphene. *Nature* **2005**, *438* (7065), 197–200.

(2) Novoselov, K. S.; Geim, A. K.; Morozov, S. V.; Jiang, D.; Zhang, Y.; Dubonos, S. V.; Grigorieva, I. V.; Firsov, A. A. Electric Field Effect in Atomically Thin Carbon Films. *Science* **2004**, *306* (5696), 666–669.

(3) Peierls, R. Quelques Propriétés Typiques Des Corps Solides. In *Annales de l'institut {Henri} {Poincaré}*; 1935; Vol. 5, pp 177–222.

(4) Landau, L. D. Zur {Theorie} Der Phasenumwandlungen {II}. *Phys. Z. Sowjetunion* **1937**, *11*, 26–35.

(5) Geim, A. K.; Novoselov, K. S. The Rise of Graphene. *Nat. Mater.* **2007**, *6* (3), 183–191.

(6) Li, D.; Kaner, R. B. Materials Science. Graphene-Based Materials. *Science* **2008**, *320* (5880), 1170–1171.

(7) Gupta, A.; Sakthivel, T.; Seal, S. Recent Development in 2D Materials Beyond Graphene. *Prog. Mater. Sci.* **2015**, *73* (February), 44–126.

(8) Kulkarni, G. S.; Reddy, K.; Zhong, Z.; Fan, X. Graphene Nanoelectronic Heterodyne Sensor for Rapid and Sensitive Vapour Detection. *Nat. Commun.* **2014**, *5*.

(9) Musso, T.; Kumar, P. V; Foster, A. S.; Grossman, J. C. Graphene Oxide as a Promising Hole Injection Layer for MoS2-Based Electronic Devices. *ACS Nano* **2014**, *8* (11), 11432–11439.

(10) Radisavljevic, B.; Radenovic, A.; Brivio, J.; Giacometti, V.; Kis, A. Single-Layer MoS2 Transistors. *Nat. Nanotechnol.* **2011**, *6* (3), 147–150.

(11) Bertolazzi, S.; Krasnozhon, D.; Kis, A. Nonvolatile Memory Cells Based on MoS2/graphene Heterostructures. *ACS Nano* **2013**, *7* (4), 3246–3252.

(12) Roy, K.; Padmanabhan, M.; Goswami, S.; Sai, T. P.; Ramalingam, G.; Raghavan, S.; Ghosh, A. Graphene-MoS2 Hybrid Structures for Multifunctional Photoresponsive Memory Devices. *Nat. Nanotechnol.* **2013**, *8* (11), 826–830.

(13) Li, S.-S.; Tu, K.-H.; Lin, C.-C.; Chen, C.-W.; Chhowalla, M. Solution-Processable Graphene Oxide as an Efficient Hole Transport Layer in Polymer Solar Cells. *ACS Nano* **2010**, *4* (6), 3169–3174.

(14) Li, Y.; Chernikov, A.; Zhang, X.; Rigosi, A.; Hill, H. M.; van der Zande, A. M.; Chenet, D. a.; Shih, E.-M.; Hone, J.; Heinz, T. F. Measurement of the Optical Dielectric Function of Monolayer Transition-Metal Dichalcogenides: MoS2, MoSe2, WS2 and WSe2. *Phys. Rev. B* **2014**, *90* (205422), 1–6.

(15) Wang, Q. H.; Kalantar-Zadeh, K.; Kis, A.; Coleman, J. N.; Strano, M. S. Electronics and Optoelectronics of Two-Dimensional Transition Metal Dichalcogenides. *Nat. Nanotechnol.* **2012**, *7* (11), 699–712.

(16) Wang, X.; Gong, Y.; Shi, G.; Chow, W. L.; Keyshar, K.; Ye, G.; Vajtai, R.; Lou, J.; Liu, Z.; Ringe, E.; Tay, B. K.; Ajayan, P. M. Chemical Vapor Deposition Growth of Crystalline Monolayer MoSe2. *ACS Nano* **2014**, *8* (5), 5125–5131.

(17) Loo, A. H.; Bonanni, A.; Sofer, Z.; Pumera, M. Exfoliated Transition Metal Dichalcogenides (MoS2, MoSe2, WS2, WSe2): An Electrochemical Impedance Spectroscopic Investigation. *Electrochem. commun.* **2015**, *50*, 39–42.

(18) Graphene patents - graphic of the day http://blog.thomsonreuters.com/index.php/graphene-patents-graphic-of-the-day/ (accessed Oct 5, 2015).

(19) Balandin, A. A. Thermal Properties of Graphene, Carbon Nanotubes and Nanostructured Carbon Materials. *Nat. Mater.* **2011**, *10*, 569–581.

(20) Bonaccorso, F.; Sun, Z.; Hasan, T.; Ferrari, A. C. Graphene Photonics and Optoelectronics. *Nat. Photonics* **2010**, *4* (9), 611–622.

(21) Yazyev, O. V. Magnetism in Disordered Graphene and Irradiated Graphite. *Phys. Rev. Lett.* **2008**, *101* (3), 037203.

(22) Yang, S.-L.; Sobota, J. A.; Howard, C. A.; Pickard, C. J.; Hashimoto, M.; Lu, D. H.; Mo, S.-K.; Kirchmann, P. S.; Shen, Z.-X. Superconducting Graphene Sheets in CaC6 Enabled by Phonon-Mediated Interband Interactions. *Nat. Commun.* **2014**, *5*, 3493.

(23) Castro, E.; Novoselov, K.; Morozov, S.; Peres, N.; Dos Santos, J.; Nilsson, J.; Guinea, F.; Geim, A.; Neto, A. Biased Bilayer Graphene: Semiconductor with a Gap Tunable by the Electric Field Effect. *Phys. Rev. Lett.* **2007**, *99* (21), 216802.

(24) Kim, C. O.; Hwang, S. W.; Kim, S.; Shin, D. H.; Kang, S. S.; Kim, J. M.; Jang, C. W.; Kim, J. H.; Lee, K. W.; Choi, S.-H.; Hwang, E. High-Performance Graphene-Quantum-Dot Photodetectors. *Sci. Rep.* **2014**, *4*, 5603.

(25) Dreyer, D. R.; Ruoff, R. S.; Bielawski, C. W. From Conception to Realization: An Historial Account of Graphene and Some Perspectives for Its Future. *Angew. Chemie - Int. Ed.* **2010**, *49* (49), 9336–9344.

(26) Parvez, K.; Wu, Z. S.; Li, R.; Liu, X.; Graf, R.; Feng, X.; Müllen, K. Exfoliation of Graphite into Graphene in Aqueous Solutions of Inorganic Salts. *J. Am. Chem. Soc.* **2014**, *136* (16), 6083–6091.

(27) Kosynkin, D. V; Higginbotham, A. L.; Sinitskii, A.; Lomeda, J. R.; Dimiev, A.; Price, B. K.; Tour, J. M. Longitudinal Unzipping of Carbon Nanotubes to Form Graphene Nanoribbons. *Nature* **2009**, *458*, 872–876.

(28) Pei, S.; Cheng, H. The Reduction of Graphene Oxide. *Carbon N. Y.* **2011**, *50* (9), 3210–3228.

(29) Wang, Y.; Zheng, Y.; Xu, X.; Dubuisson, E.; Bao, Q.; Lu, J.; Loh, K. P. Electrochemical Delamination of CVD-Grown Graphene Film: Toward the Recyclable Use of Copper Catalyst. *ACS Nano* **2011**, *5* (12), 9927–9933.

(30) Gupta, P.; Dongare, P. D.; Grover, S.; Dubey, S.; Mamgain, H.; Bhattacharya, A.; Deshmukh, M. M. A Facile Process for Soak-and-Peel Delamination of CVD Graphene from Substrates Using Water. *Sci. Rep.* **2014**, *4*, 3882.

(31) Chen, D.; Tang, L.; Li, J. Graphene-Based Materials in Electrochemistry. *Chem. Soc. Rev.* **2010**, *39* (8), 3157.

(32) Hernandez, Y.; Nicolosi, V.; Lotya, M.; Blighe, F. M.; Sun, Z.; De, S.; Mcgovern, I. T.; Holland, B.; Byrne, M.; Ko, Y. K. G. U. N.; Boland, J. J.; Niraj, P.; Duesberg, G.; Krishnamurthy, S.; Goodhue, R.; Hutchison, J.; Scardaci, V.; Ferrari, A. C.; Coleman, J. N.; Gun, Y.; Gun'Ko, Y. K.; Boland, J. J.; Niraj, P.; Duesberg, G.; Krishnamurthy, S.; Goodhue, R.; Hutchison, J.; Scardaci, V.; Ferrari, A. C.; Coleman, J. N.; Krishnamurti, S.; Goodhue, R.; Hutchison, J.; Scardaci, V.; Andrea, C.; Holland, B.; Byrne, M.; Gun, Y.; Boland, J. J.; Niraj, P.; Duesberg, G.; Krishnamurthy, S.; Goodhue, R.; Hutchison, J.; Scardaci, V.; Ferrari, A. C.; Coleman, J. N. High-Yield Production of Graphene by Liquid-Phase Exfoliation of Graphite. *Nat. Nanotechnol.* **2008**, *3* (9), 563–568.

(33) Lotya, M.; King, P. J.; Khan, U.; De, S.; Coleman, J. N. High-Concentration, Surfactant-Stabilized Graphene Dispersions. *ACS Nano* **2010**, *4* (6), 3155–3162.

(34) Khan, U.; O'Neill, A.; Lotya, M.; De, S.; Coleman, J. High Concentration Solvent Exfoliation of Graphene. *Small* **2010**, 1–4.

(35) Zhu, B. Y.; Murali, S.; Cai, W.; Li, X.; Suk, J. W.; Potts, J. R.; Ruoff, R. S.; Zhu, Y.; Murali, S.; Cai, W.; Li, X.; Suk, J. W.; Potts, J. R.; Ruoff, R. S. Graphene and Graphene Oxide: Synthesis, Properties, and Applications. *Adv. Mater.* **2010**, *22* (35), 3906–3924.

(36) Rümmeli, M. H.; Rocha, C. G.; Ortmann, F.; Ibrahim, I.; Sevincli, H.; Börrnert, F.; Kunstmann, J.; Bachmatiuk, A.; Pötschke, M.; Shiraishi, M.; Meyyappan, M.; Büchner,

B.; Roche, S.; Cuniberti, G. Graphene: Piecing It Together. *Adv. Mater.* **2011**, *23* (39), 4471–4490.

(37) Graphene supermarket http://www.graphene-supermarket.com. (accessed Oct 14, 2013).

(38) Reina, A.; Jia, X.; Ho, J.; Nezich, D.; Son, H.; Bulovic, V.; Dresselhaus, M. S.; Kong, J. Large Area, Few-Layer Graphene Films on Arbitrary Substrates by Chemical Vapor Deposition. *Nano Lett.* **2009**, *9* (1), 30–35.

(39) Li, X.; Cai, W.; An, J.; Kim, S.; Nah, J.; Yang, D.; Piner, R.; Velamakanni, A.; Jung, I.; Tutuc, E.; Banerjee, S. K.; Colombo, L.; Ruoff, R. S. Large-Area Synthesis of High-Quality and Uniform Graphene Films on Copper Foils. *Science* **2009**, *324* (5932), 1312–1314.

(40) Li, X.; Magnuson, C. W.; Venugopal, A.; Tromp, R. M.; Hannon, J. B.; Vogel, E. M.; Colombo, L.; Ruoff, R. S. Large-Area Graphene Single Crystals Grown by Low-Pressure Chemical Vapor Deposition of Methane on Copper. *J. Am. Chem. Soc.* **2011**, *133* (9), 2816–2819.

(41) Zurutuza, A.; Marinelli, C. Challenges and Opportunities in Graphene Commercialization. *Nat. Nanotechnol.* **2014**, *9* (10), 730–734.

(42) Chabot, V.; Higgins, D.; Yu, A.; Xiao, X.; Chen, Z.; Zhang, J. A Review of Graphene and Graphene Oxide Sponge: Material Synthesis and Applications to Energy and the Environment. *Energy Environ. Sci.* **2014**, *7* (5), 1564.

(43) Abbas, A. N.; Liu, G.; Liu, B.; Zhang, L.; Liu, H.; Ohlberg, D.; Wu, W.; Zhou, C. Patterning, Characterization, and Chemical Sensing Applications of Graphene Nanoribbon Arrays down to 5 Nm Using Helium Ion Beam Lithography. *ACS Nano* **2014**, *8* (2), 1538–1546.

(44) Xu, Y.; Shi, G.; Duan, X. Self-Assembled Three-Dimensional Graphene Macrostructures: Synthesis and Applications in Supercapacitors. *Acc. Chem. Res.* **2015**, *48* (6), 1666–1675.

(45) Renteria, J.; Nika, D.; Balandin, A. Graphene Thermal Properties: Applications in Thermal Management and Energy Storage. *Appl. Sci.* **2014**, *4* (4), 525–547.

(46) Yin, Z.; Zhu, J.; He, Q.; Cao, X.; Tan, C.; Chen, H.; Yan, Q.; Zhang, H. Graphene-Based Materials for Solar Cell Applications. *Adv. Energy Mater.* **2014**, *4* (1), 1–19.

(47) Grigorenko, A. N.; Polini, M.; Novoselov, K. S. Graphene Plasmonics. *Nat. Photonics* **2012**, *6* (11), 749–758.

(48) Hu, J.; Odom, T. W.; Lieber, C. M. Chemistry and Physics in One Dimension: Synthesis and Properties of Nanowires and Nanotubes. *Acc. Chem. Res.* **1999**, *32* (5), 435–445.

(49) Gan, X.; Shiue, R.-J.; Gao, Y.; Meric, I.; Heinz, T. F.; Shepard, K.; Hone, J.; Assefa, S.; Englund, D. Chip-Integrated Ultrafast Graphene Photodetector with High Responsivity. *Nat. Photonics* **2013**, *7*, 883–887.

(50) Lee, W.-Y.; Yang, S.-Y.; Jeon, J.-N.; Cho, Y. J.; Kwon, Y.; Kim, Y.-S. P-94: Ultra-Thin Graphene Oxide/Polymer Multi-Layer Encapsulation for Flexible OLED Displays. *SID Symp. Dig. Tech. Pap.* **2014**, *45* (1), 1340–1343.

(51) Yu, A.; Roes, I.; Davies, A.; Chen, Z. Ultrathin, Transparent, and Flexible Graphene Films for Supercapacitor Application. *Appl. Phys. Lett.* **2010**, *96* (25), 253105.

(52) El-Kady, M. F.; Strong, V.; Dubin, S.; Kaner, R. B. Laser Scribing of High-Performance and Flexible Graphene-Based Electrochemical Capacitors. *Science (80-.).* **2012**, *335* (6074), 1326–1330.

(53) Russo, P.; Hu, A.; Compagnini, G. Synthesis, Properties and Potential Applications of Porous Graphene: A Review. *Nano-Micro Lett.* **2013**, *5* (October), 260–273.

(54) Zhu, J.; Yang, D.; Yin, Z.; Yan, Q.; Zhang, H. Graphene and Graphene-Based Materials for Energy Storage Applications. *Small* **2014**, No. 17, 1–19.

(55) Son, D. I.; Kim, T. W.; Shim, J. H.; Jung, J. H.; Lee, D. U.; Lee, J. M.; Park, W. Il; Choi, W. K. Flexible Organic Bistable Devices Based on Graphene Embedded in an Insulating Poly(methyl Methacrylate) Polymer Layer. *Nano Lett.* **2010**, *10* (7), 2441–2447.

(56) Tang, L.; Ji, R.; Cao, X.; Lin, J.; Jiang, H.; Li, X.; Teng, K. S.; Luk, C. M.; Zeng, S.; Hao, J.; Lau, S. P. Deep Ultraviolet Photoluminescence of Water-Soluble Self-Passivated Graphene Quantum Dots. *ACS Nano* **2012**, *6* (6), 5102–5110.

(57) Jun, B.-H.; Hwang, D. W.; Jung, H. S.; Jang, J.; Kim, H.; Kang, H.; Kang, T.; Kyeong, S.; Lee, H.; Jeong, D. H.; Kang, K. W.; Youn, H.; Lee, D. S.; Lee, Y.-S. Ultrasensitive, Biocompatible, Quantum-Dot-Embedded Silica Nanoparticles for Bioimaging. *Adv. Funct. Mater.* **2012**, *22* (9), 1843–1849.

(58) Liu, Z.; Lau, S. P.; Yan, F. Functionalized Graphene and Other Two-Dimensional Materials for Photovoltaic Devices: Device Design and Processing. *Chem. Soc. Rev.* **2015**, *44* (15), 5638–5679.

(59) Zhang, Q.; Jie, J.; Diao, S.; Shao, Z.; Zhang, Q.; Wang, L.; Deng, W.; Hu, W.; Xia, H.; Yuan, X.; Lee, S.-T. Solution-Processed Graphene Quantum Dot Deep-UV Photodetectors. *ACS Nano* **2015**, *9* (2), 1561–1570.

(60) Zubair, M.; Mustafa, M.; Lee, K.; Yoon, C.; Doh, Y. H.; Choi, K. H. Fabrication of CdSe/ZnS Quantum Dots Thin Film by Electrohydrodynamics Atomization Technique for Solution Based Flexible Hybrid OLED Application. *Chem. Eng. J.* **2014**, *253* (2014), 325–331.

(61) Ritter, K. A.; Lyding, J. W. The Influence of Edge Structure on the Electronic Properties of Graphene Quantum Dots and Nanoribbons. *Nat. Mater.* **2009**, *8* (3), 235–242.

(62) Dong, Y.; Chen, C.; Zheng, X.; Gao, L.; Cui, Z.; Yang, H.; Guo, C.; Chi, Y.; Li, C. M. One-Step and High Yield Simultaneous Preparation of Single- and Multi-Layer Graphene Quantum Dots from CX-72 Carbon Black. *J. Mater. Chem.* **2012**, *22* (18), 8764.

(63) Yang, F.; Zhao, M.; Zheng, B.; Xiao, D.; Wu, L.; Guo, Y. Influence of pH on the Fluorescence Properties of Graphene Quantum Dots Using Ozonation Pre-Oxide Hydrothermal Synthesis. *J. Mater. Chem.* **2012**, *22* (48), 25471.

(64) Feng, L.; Tang, X.-Y.; Zhong, Y.-X.; Liu, Y.-W.; Song, X.-H.; Deng, S.-L.; Xie, S.-Y.; Yan, J.-W.; Zheng, L.-S. Ultra-Bright Alkylated Graphene Quantum Dots. *Nanoscale* **2014**, *6* (21), 12635–12643.

(65) Shinde, D. B.; Pillai, V. K.; Nanotubes, M. C.; Shinde, D. B.; Pillai, V. K. Electrochemical Preparation of Luminescent Graphene Quantum Dots from Multiwalled Carbon Nanotubes. *Chem. - A Eur. J.* **2012**, *18* (39), 12522–12528.

(66) Li, L.-L.; Ji, J.; Fei, R.; Wang, C.-Z.; Lu, Q.; Zhang, J.-R.; Jiang, L.-P.; Zhu, J.-J. A Facile Microwave Avenue to Electrochemiluminescent Two-Color Graphene Quantum Dots. *Adv. Funct. Mater.* **2012**, *22* (14), 2971–2979.

(67) Ponomarenko, L. A.; Schedin, F.; Katsnelson, M. I.; Yang, R.; Hill, E. W.; Novoselov, K. S.; Geim, A. K. Chaotic Dirac Billiard in Graphene Quantum Dots. *Science* **2008**, *320* (5874), 356–358.

(68) Pan, D.; Zhang, J.; Li, Z.; Wu, M. Hydrothermal Route for Cutting Graphene Sheets into Blue-Luminescent Graphene Quantum Dots. *Adv. Mater.* **2010**, *22* (6), 734–738.

(69) Liu, R.; Wu, D.; Feng, X.; Müllen, K. Bottom-Up Fabrication of Photoluminescent Graphene Quantum Dots with Uniform Morphology. *J. Am. Chem. Soc.* **2011**, *133* (39), 15221–15223.

(70) Yan, X.; Cui, X.; Li, L.-S. S. Synthesis of Large, Stable Colloidal Graphene Quantum Dots with Tunable Size. *J. Am. Chem. Soc.* **2010**, *132* (17), 5944–5945.

(71) Habiba, K.; Makarov, V. I.; Avalos, J.; Guinel, M. J. F.; Weiner, B. R.; Morell, G. Luminescent Graphene Quantum Dots Fabricated by Pulsed Laser Synthesis. *Carbon N. Y.* **2013**, *64*, 341–350.

(72) Ye, R.; Xiang, C.; Lin, J.; Peng, Z.; Huang, K.; Yan, Z.; Cook, N. P.; Samuel, E. L. G.; Hwang, C.-C.; Ruan, G.; Ceriotti, G.; Raji, A.-R. O.; Martí, A. A.; Tour, J. M. Coal as an Abundant Source of Graphene Quantum Dots. *Nat. Commun.* **2013**, *4*, 2943.

(73) Huang, Z.; Shen, Y.; Li, Y.; Zheng, W.; Xue, Y.; Qin, C.; Zhang, B.; Hao, J.; Feng, W. Facile Synthesis of Analogous Graphene Quantum Dots with sp(2) Hybridized Carbon Atom Dominant Structures and Their Photovoltaic Application. *Nanoscale* **2014**, *6* (21), 13043–13052.

(74) Lu, J.; Yeo, P. S. E.; Gan, C. K.; Wu, P.; Loh, K. P. Transforming C60 Molecules into Graphene Quantum Dots. *Nat. Nanotechnol.* **2011**, *6* (4), 247–252.

(75) Dong, Y.; Li, G.; Zhou, N.; Wang, R.; Chi, Y.; Chen, G. Graphene Quantum Dot as a Green and Facile Sensor for Free Chlorine in Drinking Water. *Anal. Chem.* **2012**, *84* (19), 8378–8382.

(76) Bao, Q.; Loh, K. P. Graphene Photonics, Plasmonics, and Broadband Optoelectronic Devices. *ACS Nano*. May 22, 2012, pp 3677–3694.

(77) Brar, V. W.; Jang, M. S.; Sherrott, M.; Lopez, J. J.; Atwater, H. a. Highly Confined Tunable Mid-Infrared Plasmonics in Graphene Nanoresonators. *Nano Lett.* **2013**, *13* (6), 2541–2547.

(78) Youn, D.-H.; Yu, Y.-J.; Choi, H.; Kim, S.-H.; Choi, S.-Y.; Choi, C.-G. Graphene Transparent Electrode for Enhanced Optical Power and Thermal Stability in GaN Light-Emitting Diodes. *Nanotechnology* **2013**, *24* (7), 075202.

(79) Lin, J.; Raji, A.-R. O.; Nan, K.; Peng, Z.; Yan, Z.; Samuel, E. L. G.; Natelson, D.; Tour, J. M. Iron Oxide Nanoparticle and Graphene Nanoribbon Composite as an Anode Material for High-Performance Li-Ion Batteries. *Adv. Funct. Mater.* **2014**, *24* (14), 2044–2048.

(80) Kholmanov, I. N.; Domingues, S. H.; Chou, H.; Wang, X.; Tan, C.; Kim, J.-Y. Y.; Li, H.; Piner, R.; Zarbin, A. J. G.; Ruoff, R. S. Reduced Graphene Oxide/copper Nanowire

Hybrid Films as High-Performance Transparent Electrodes. *ACS Nano* **2013**, *7* (2), 1811–1816.

(81) Xu, F.; Chen, J.; Wu, X.; Zhang, Y.; Wang, Y.; Sun, J.; Bi, H.; Lei, W.; Ni, Y.; Sun, L. Graphene Scaffolds Enhanced Photogenerated Electron Transport in ZnO Photoanodes for High-Efficiency Dye-Sensitized Solar Cells. *J. Phys. Chem. C* **2013**, *117* (17), 8619–8627.

(82) Joshua Yang, J.; Miao, F.; Pickett, M. D.; Ohlberg, D. a a; Stewart, D. R.; Lau, C. N.; Williams, R. S. The Mechanism of Electroforming of Metal Oxide Memristive Switches. *Nanotechnology* **2009**, *20* (21), 215201.

(83) Waser, R. Electrochemical and Thermochemical Memories. In *2008 IEEE International Electron Devices Meeting*; IEEE, 2008; pp 1–4.

(84) Waser, R.; Aono, M. Nanoionics-Based Resistive Switching Memories. *Nat. Mater.* **2007**, *6* (11), 833–840.

(85) Wagenaar, J. J. T.; Morales-Masis, M.; van Ruitenbeek, J. M. Observing “quantized” Conductance Steps in Silver Sulfide: Two Parallel Resistive Switching Mechanisms. *J. Appl. Phys.* **2012**, *111* (1), 014302.

(86) Suga, T.; Aoki, K.; Nishide, H. Ionic Liquid-Triggered Redox Molecule Placement in Block Copolymer Nanotemplates toward an Organic Resistive Memory. *ACS Macro Lett.* **2015**, *4* (9), 892–896.

(87) Mohapatra, S. R.; Tsuruoka, T.; Krishnan, K.; Hasegawa, T.; Aono, M. Effects of Temperature and Ambient Pressure on the Resistive Switching Behaviour of Polymer-Based Atomic Switches. *J. Mater. Chem. C* **2015**, *3* (22), 5715–5720.

(88) Prezioso, M.; Merrikh-Bayat, F.; Hoskins, B. D.; Adam, G. C.; Likharev, K. K.; Strukov, D. B. Training and Operation of an Integrated Neuromorphic Network Based on Metal-Oxide Memristors. *Nature* **2015**, *521* (7550), 61–64.

(89) Schindler, C.; Thermadam, S. C. P.; Waser, R.; Kozicki, M. N. Bipolar and Unipolar Resistive Switching in Cu-Doped SiO2. *IEEE Trans. Electron Devices* **2007**, *54* (10), 2762–2768.

(90) Kim, S.; Park, J.; Jung, S.; Lee, W.; Woo, J.; Cho, C.; Siddik, M.; Shin, J.; Park, S.; Hun Lee, B.; Hwang, H. Excellent Resistive Switching in Nitrogen-Doped Ge2Sb2Te5 Devices for Field-Programmable Gate Array Configurations. *Appl. Phys. Lett.* **2011**, *99* (19), 192110.

(91) Park, S.; Park, D.; Jeong, K.; Kim, T.; Park, S.; Ahn, M.; Yang, W. J.; Han, J. H.; Jeong, H. S.; Jeon, S. G.; Song, J. Y.; Cho, M.-H. Effect of the Thermal Conductivity on Resistive Switching in GeTe and Ge 2 Sb 2 Te 5 Nanowires. *ACS Appl. Mater. Interfaces* **2015**, *7* (39), 21819–21827.

(92) Wouters, D. J.; Waser, R.; Wuttig, M. Phase-Change and Redox-Based Resistive Switching Memories. *Proc. IEEE* **2015**, *103* (8), 1274–1288.

(93) Choi, S. J.; Kim, J. H.; Lee, H. H. Deep-UV Curing of poly(4-Vinyl Phenol) Gate Dielectric for Hysteresis-Free Organic Thin-Film Transistors. *IEEE Electron Device Lett.* **2009**, *30* (5), 454–456.

(94) Lee, I.; Park, H.-Y.; Park, J. J.-H. J.; Yoo, G.; Lim, M.-H.; Park, J. J.-H. J.; Rathi, S.; Jung, W.-S.; Kim, J.; Kim, S.-W.; Roh, Y.; Kim, G.-H.; Park, J. J.-H. J. Poly-4-Vinylphenol and Poly(melamine-Co-Formaldehyde)-Based Graphene Passivation Method for Flexible, Wearable and Transparent Electronics. *Nanoscale* **2014**, *6* (7), 3830–3836.

(95) Mamo, M. A.; Sustaita, A. O.; Coville, N. J.; Hümmelgen, I. A. Polymer Composite of Poly(vinyl Phenol)-Reduced Graphene Oxide Reduced by Vitamin C in Low Energy Consuming Write-Once–read-Many Times Memory Devices. *Org. Electron.* **2013**, *14* (1), 175–181.

(96) Ouyang, J. Polymer:nanoparticle Memory Devices with Electrode-Sensitive Bipolar Resistive Switches by Exploring the Electrical Contact between a Bulk Metal and Metal Nanoparticles. *Org. Electron. physics, Mater. Appl.* **2013**, *14* (2), 665–675.

(97) Kim, H.-J.; Jung, S. M.; Kim, Y.-H.; Kim, B.-J.; Ha, S.; Kim, Y.-S.; Yoon, T.-S.; Lee, H. H. Characterization of Gold Nanoparticle Pentacene Memory Device with Polymer Dielectric Layer. *Thin Solid Films* **2011**, *519* (18), 6140–6143.

(98) Choi, K. H.; Ali, J.; Doh, Y. H. Exploring Resistive Switching in poly(4-Vinylphenol)–graphene Nano-Composite Films. *Jpn. J. Appl. Phys.* **2015**, *54* (3), 035103.

(99) Hirose, Y.; Hirose, H. POLARITY-DEPENDENT MEMORY SWITCHING AND BEHAVIOR OF Ag DENDRITE IN Ag-PHOTODOPED AMORPHOUS As//2S//3 FILMS. *J. Appl. Phys.* **1976**, *47*, 2767–2772.

(100) Choi, K.-H. H.; Duraisamy, N.; Awais, M. N.; Malik Muhammad, N.; Kim, H.-C. C.; Jo, J.; Naeem, M.; Malik, N.; Muhammad, N. M.; Kim, H.-C. C.; Jo, J. Investigation on Switching Behavior of ZrO2 Thin Film for Memory Device Applications. *Mater. Sci. Semicond. Process.* **2013**, *16* (5), 1285–1291.

(101) He, C. L.; Zhuge, F.; Zhou, X. F.; Li, M.; Zhou, G. C.; Liu, Y. W.; Wang, J. Z.; Chen, B.; Su, W. J.; Liu, Z. P.; Wu, Y. H.; Cui, P.; Li, R. W. Nonvolatile Resistive Switching in Graphene Oxide Thin Films. *Appl. Phys. Lett.* **2009**, *95*.

(102) Mustafa, M.; Awais, M. N.; Pooniah, G.; Choi, K. H.; Ko, J.; Doh, Y. H. Electrospray Deposition of a Graphene-Oxide Thin Film, Its Characterization and Investigation of Its Resistive Switching Performance. *Journal of the Korean Physical Society*. December 2012, pp 470–475.

(103) Muhammad, N. M.; Duraisamy, N.; Rahman, K.; Dang, H. W.; Jo, J.; Choi, K. H. Fabrication of Printed Memory Device Having Zinc-Oxide Active Nano-Layer and Investigation of Resistive Switching. *Curr. Appl. Phys.* **2013**, *13* (1), 90–96.

(104) Nanoislands, Z.; Qi, J.; Olmedo, M.; Ren, J.; Zhan, N.; Zhao, J.; Zheng, J.; Liu, J. Resistive Switching in Single Epitaxial. **2012**, No. 2, 1051–1058.

(105) Choi, K. H. H.; Ali, J.; Na, K.-H. Fabrication of Graphene-nanoflake/poly(4-Vinylphenol) Polymer Nanocomposite Thin Film by Electrohydrodynamic Atomization and Its Application as Flexible Resistive Switching Device. *Phys. B Condens. Matter* **2015**, *475*, 148–155.

(106) Awais, M. N.; Choi, K. H. Resistive Switching in a Printed Nanolayer of Poly(4-Vinylphenol). *J. Electron. Mater.* **2013**, *42* (6), 1202–1208.

(107) Joo, W. J.; Choi, T. L.; Lee, K. H.; Chung, Y. Study on Threshold Behavior of Operation Voltage in Metal Filament-Based Polymer Memory. *J. Phys. Chem. B* **2007**, *111* (27), 7756–7760.

(108) Yang, Y. C.; Pan, F.; Zeng, F.; Liu, M. Switching Mechanism Transition Induced by Annealing Treatment in Nonvolatile Cu/ZnO/Cu/ZnO/Pt Resistive Memory: From Carrier Trapping/detrapping to Electrochemical Metallization. *J. Appl. Phys.* **2009**, *106* (12), 123705.

(109) Bozano, L. D.; Kean, B. W.; Beinhoff, M.; Carter, K. R.; Rice, P. M.; Scott, J. C. Organic Materials and Thin-Film Structures for Cross-Point Memory Cells Based on Trapping in Metallic Nanoparticles. *Adv. Funct. Mater.* **2005**, *15* (12), 1933–1939.

(110) Hwang, S. K.; Lee, J. M.; Kim, S. O. S. O.; Park, J. S.; Park, H. Il; Ahn, C. W.; Lee, K. J.; Lee, T.; Kim, S. O. S. O. Flexible Multilevel Resistive Memory with Controlled Charge Trap B- and N-Doped Carbon Nanotubes. *Nano Lett.* **2012**, *12* (5), 2217–2221.

(111) Lee, M.-J.; Kim, S. I.; Lee, C. B.; Yin, H.; Ahn, S.-E.; Kang, B. S.; Kim, K. H.; Park, J. C.; Kim, C. J.; Song, I.; Kim, S. W.; Stefanovich, G.; Lee, J. H.; Chung, S. J.; Kim, Y. H.; Park, Y. Low-Temperature-Grown Transition Metal Oxide Based Storage Materials and Oxide Transistors for High-Density Non-Volatile Memory. *Adv. Funct. Mater.* **2009**, *19* (10), 1587–1593.

(112) Chen, J.-Y.; Hsin, C.-L.; Huang, C.-W.; Chiu, C.-H.; Huang, Y.-T.; Lin, S.-J.; Wu, W.-W.; Chen, L.-J. Dynamic Evolution of Conducting Nanofilament in Resistive Switching Memories. *Nano Lett.* **2013**, *13* (8), 3671–3677.

(113) Kim, J.; Ko, C.; Frenzel, A.; Ramanathan, S.; Hoffman, J. E. Nanoscale Imaging and Control of Resistance Switching in VO2 at Room Temperature. *Appl. Phys. Lett.* **2010**, *96* (21), 10–13.

(114) Liu, X.; Sadaf, S. M.; Son, M.; Shin, J.; Park, J.; Lee, J.; Park, S.; Hwang, H. Diode-Less Bilayer Oxide (WO X –NbO X) Device for Cross-Point Resistive Memory Applications. *Nanotechnology* **2011**, *22* (47), 475702.

(115) Sebastian, A.; Pauza, A.; Rossel, C.; Shelby, R. M.; Rodríguez, A. F.; Pozidis, H.; Eleftheriou, E. Resistance Switching at the Nanometre Scale in Amorphous Carbon. *New J. Phys.* **2011**, *13* (1), 013020.

(116) Ling, Q. D.; Lim, S. L.; Song, Y.; Zhu, C. X.; Chan, D. S. H.; Kang, E. T.; Neoh, K. G. Nonvolatile Polymer Memory Device Based on Bistable Electrical Switching in a Thin Film of poly(N-Vinylcarbazole) with Covalently Bonded C60. *Langmuir* **2007**, *23* (1), 312–319.

(117) Gao, S.; Song, C.; Chen, C.; Zeng, F.; Pan, F. Dynamic Processes of Resistive Switching in Metallic Filament-Based Organic Memory Devices. *J. Phys. Chem. C* **2012**, *116* (33), 17955–17959.

(118) Chen, G.; Song, C.; Chen, C.; Gao, S.; Zeng, F.; Pan, F. Resistive Switching and Magnetic Modulation in Cobalt-Doped ZnO. *Adv. Mater.* **2012**, *24* (26), 3515–3520.

(119) Jo, S. H.; Chang, T.; Ebong, I.; Bhadviya, B. B.; Mazumder, P.; Lu, W. Nanoscale Memristor Device as Synapse in Neuromorphic Systems. *Nano Lett.* **2010**, *10* (4), 1297–1301.

(120) Borghetti, J.; Snider, G. S.; Kuekes, P. J.; Yang, J. J.; Stewart, D. R.; Williams, R. S. "Memristive" Switches Enable "Stateful" Logic Operations via Material Implication. *Nature* **2010**, *464* (7290), 873–876.

(121) Muratore, C.; Hu, J. J.; Wang, B.; Haque, M. a.; Bultman, J. E.; Jespersen, M. L.; Shamberger, P. J.; McConney, M. E.; Naguy, R. D.; Voevodin, a. a. Continuous Ultra-Thin MoS2 Films Grown by Low-Temperature Physical Vapor Deposition. *Appl. Phys. Lett.* **2014**, *104* (26), 1–6.

(122) Kang, B.-M.; Jeong, W.-J.; Park, G.-C.; Yoon, D.-J.; Ahn, H.-G.; Lim, Y.-S. The Characteristics of an Antibacterial TiAgN Thin Film Coated by Physical Vapor Deposition Technique. *J. Nanosci. Nanotechnol.* **2015**, *15* (8), 6020–6023.

(123) Wei, D.; Liu, Y.; Wang, Y.; Zhang, H.; Huang, L.; Yu, G. Synthesis of N-Doped Graphene by Chemical Vapor Deposition and Its Electrical Properties. *Nano Lett.* **2009**, *9*, 1752–1758.

(124) Song, X.; Gao, J.; Nie, Y.; Gao, T.; Sun, J.; Ma, D.; Li, Q.; Chen, Y.; Jin, C.; Bachmatiuk, A.; Rümmeli, M. H.; Ding, F.; Zhang, Y.; Liu, Z. Chemical Vapor Deposition Growth of Large-Scale Hexagonal Boron Nitride with Controllable Orientation. *Nano Res.* **2015**, *8* (10), 3164–3176.

(125) Müller, F.; Lessel, M.; Grandthyll, S.; Jacobs, K.; Hüfner, S.; Gsell, S.; Weinl, M.; Schreck, M. Increasing the Wear Resistance by Interstitial Alloying with Boron via Chemical Vapor Deposition. *Langmuir* **2013**, *29* (14), 4543–4550.

(126) Bachmatiuk, a; Abelin, R. F.; Quang, H. T.; Trzebicka, B.; Eckert, J.; Rummeli, M. H. Chemical Vapor Deposition of Twisted Bilayer and Few-Layer MoSe2 over SiO X Substrates. *Nanotechnology* **2014**, *25* (36), 365603.

(127) Quan, X.-T.; Zhu, H.-C.; Cai, H.-T.; Zhang, J.-Q.; Wang, X.-J. Resistive Switching Behavior in Amorphous Aluminum Oxide Film Grown by Chemical Vapor Deposition. *Chinese Phys. Lett.* **2014**, *31* (7), 078101.

(128) Schwartzkopf, M.; Buffet, A.; Körstgens, V.; Metwalli, E.; Schlage, K.; Benecke, G.; Perlich, J.; Rawolle, M.; Rothkirch, A.; Heidmann, B.; Herzog, G.; Müller-Buschbaum, P.; Röhlsberger, R.; Gehrke, R.; Stribeck, N.; Roth, S. V. From Atoms to Layers: In Situ Gold Cluster Growth Kinetics during Sputter Deposition. *Nanoscale* **2013**, *5* (11), 5053–5062.

(129) Gerdes, H.; Bandorf, R.; Loch, D.; Bräuer, G. Reactive Sputter Deposition of Alumina Coatings. *IOP Conf. Ser. Mater. Sci. Eng.* **2012**, *39*, 012009.

(130) Simon, A. H. Sputter Processing. In *Handbook of Thin Film Deposition (Third Edition)*; 2012; pp 55–88.

(131) Elayaraja, K.; Chandra, V. S.; Joshy, M. I. A.; Suganthi, R. V; Asokan, K.; Kalkura, S. N. Nanocrystalline Biphasic Resorbable Calcium Phosphate (HAp/β-TCP) Thin Film Prepared by Electron Beam Evaporation Technique. *Appl. Surf. Sci.* **2013**, *274*, 203–209.

(132) Marvel, R. E.; Appavoo, K.; Choi, B. K.; Nag, J.; Haglund, R. F. Electron-Beam Deposition of Vanadium Dioxide Thin Films. *Appl. Phys. A Mater. Sci. Process.* **2013**, *111*, 975–981.

(133) Blackwell, S.; Smith, R.; Kenny, S. D.; Walls, J. M. Modeling Evaporation, Ion-Beam Assist, and Magnetron Sputtering of Thin Metal Films over Realistic Time Scales. *Phys. Rev. B - Condens. Matter Mater. Phys.* **2012**, *86* (3), 1–12.

(134) Arthur, J. R. Molecular Beam Epitaxy. *Surf. Sci.* **2002**, *500*, 189–217.

(135) Lin, M.-Y.; Guo, W.-C.; Wu, M.-H.; Wang, P.-Y.; Liu, T.-H.; Pao, C.-W.; Chang, C.-C.; Lee, S.-C.; Lin, S.-Y. Low-Temperature Grown Graphene Films by Using Molecular Beam Epitaxy. *Appl. Phys. Lett.* **2012**, *101* (22), 221911.

(136) Hayashi, I. Molecular Beam Epitaxy. *Shinku* **1973**, *16* (3), 91–95.

(137) Knodle, W. S.; Chow, R. Molecular Beam Epitaxy. In *Handbook of Thin Film Deposition Processes and Techniques*; Elsevier, 2001; pp 381–461.

(138) Abadi, M. H. S.; Hamidon, M. N.; Shaari, A. H.; Abdullah, N.; Wagiran, R. SnO2/Pt Thin Film Laser Ablated Gas Sensor Array. *Sensors* **2011**, *11* (8), 7724–7735.

(139) Miyaji, G.; Miyazaki, K. Origin of Periodicity in Nanostructuring on Thin Film Surfaces Ablated with Femtosecond Laser Pulses. *Opt. Express* **2008**, *16* (20), 16265–16271.

(140) Liu, C.; Choi, J. Precision Patterning of Conductive Polymer Nanocomposite Using a Laser-Ablated Thin Film. *J. Micromechanics Microengineering* **2012**, *22* (4), 045014.

(141) Shah, A.; Moulin, E.; Ballif, C. Technological Status of Plasma-Deposited Thin-Film Silicon Photovoltaics. *Sol. Energy Mater. Sol. Cells* **2013**, *119*, 311–316.

(142) Chen, R. T.; Muir, B. W.; Such, G. K.; Postma, A.; Evans, R. a.; Pereira, S. M.; McLean, K. M.; Caruso, F. Surface "Click" Chemistry on Brominated Plasma Polymer Thin Films. *Langmuir* **2010**, *26* (5), 3388–3393.

(143) Kakiuchi, H.; Ohmi, H.; Yasutake, K. Atmospheric-Pressure Low-Temperature Plasma Processes for Thin Film Deposition. *J. Vac. Sci. Technol. A Vacuum, Surfaces, Film.* **2014**, *32* (3), 030801.

(144) Tynell, T.; Karppinen, M. Atomic Layer Deposition of ZnO: A Review. *Semicond. Sci. Technol.* **2014**, *29*, 043001.

(145) Sutherland, B. R.; Hoogland, S.; Adachi, M. M.; Kanjanaboos, P.; Wong, C. T. O.; McDowell, J. J.; Xu, J.; Voznyy, O.; Ning, Z.; Houtepen, A. J.; Sargent, E. H. Perovskite Thin Films via Atomic Layer Deposition. *Adv. Mater.* **2014**, *27* (1), 53–58.

(146) Sajid, M.; Zubair, M.; Doh, Y. H.; Na, K.-H.; Choi, K. H. Flexible Large Area Organic Light Emitting Diode Fabricated by Electrohydrodynamics Atomization Technique. *J. Mater. Sci. Mater. Electron.* **2015**, *26* (9), 7192–7199.

(147) Muhammad, N. M.; Naeem, A. M.; Duraisamy, N.; Kim, D.-S.; Choi, K.-H. Fabrication of High Quality Zinc-Oxide Layers through Electrohydrodynamic Atomization. *Thin Solid Films* **2012**, *520* (6), 1751–1756.

(148) Wang, K.; Stark, J. P. W.; Stark, K. W. J. P. W. Deposition of Colloidal Gold Nanoparticles by Fully Pulsed-Voltage-Controlled Electrohydrodynamic Atomisation. *J. Nanoparticle Res.* **2009**, *12* (3), 707–711.

(149) Ali, A.; Ali, K.; Kwon, K. R.; Hyun, M. T.; Choi, K. H. Electrohydrodynamic Atomization Approach to Graphene/zinc Oxide Film Fabrication for Application in Electronic Devices. *J. Mater. Sci. Mater. Electron.* **2014**, *25* (2), 1097–1104.

(150) Ali, K.; Ali, J.; Mehdi, S. M.; Choi, K.-H.; Yang, Y. J. Rapid Fabrication of Al2O3 Encapsulations for Organic Electronic Devices. *Appl. Surf. Sci.* **2015**, *353*, 1186–1194.

(151) Ghoneim, M.; Hussain, M. Review on Physically Flexible Nonvolatile Memory for Internet of Everything Electronics. *Electronics* **2015**, *4* (3), 424–479.

(152) Galagan, Y.; Coenen, E. W. C.; Abbel, R.; van Lammeren, T. J.; Sabik, S.; Barink, M.; Meinders, E. R.; Andriessen, R.; Blom, P. W. M. Photonic Sintering of Inkjet Printed Current Collecting Grids for Organic Solar Cell Applications. *Org. Electron.* **2013**, *14* (1), 38–46.

(153) Azzellino, G.; Grimoldi, A.; Binda, M.; Caironi, M.; Natali, D.; Sampietro, M. Fully Inkjet-Printed Organic Photodetectors with High Quantum Yield. *Adv. Mater.* **2013**, *25* (47), 6829–6833.

(154) Someya, T. *Stretchable Electronics*; John Wiley & Sons, 2012.

(155) Khan, S.; Lorenzelli, L.; Dahiya, R. S. Technologies for Printing Sensors and Electronics Over Large Flexible Substrates: A Review. *IEEE Sens. J.* **2015**, *15* (6), 3164–3185.

(156) Chen, P.; Chen, H.; Qiu, J.; Zhou, C. Inkjet Printing of Single-Walled Carbon nanotube/RuO2 Nanowire Supercapacitors on Cloth Fabrics and Flexible Substrates. *Nano Res.* **2010**, *3* (8), 594–603.

(157) Yeo, J.; Kim, G.; Hong, S.; Kim, M. S.; Kim, D.; Lee, J.; Lee, H. B.; Kwon, J.; Suh, Y. D.; Kang, H. W.; Sung, H. J.; Choi, J.-H.; Hong, W.-H.; Ko, J. M.; Lee, S.-H.; Choa, S.-

H.; Ko, S. H. Flexible Supercapacitor Fabrication by Room Temperature Rapid Laser Processing of Roll-to-Roll Printed Metal Nanoparticle Ink for Wearable Electronics Application. *J. Power Sources* **2014**, *246* (2014), 562–568.

(158) Poon, H. F. Electrohydrodynamic Printing, Princeton University, 2002.

(159) Duraisamy, N.; Muhammad, N. M.; Hyun, M. T.; Choi, K. H. Structural and Electrical Properties of P3HT:PCBM/PEDOT:PSS Thin Films Deposited through Electrohydrodynamic Atomization Technique. *Mater. Lett.* **2013**, *92*, 227–230.

(160) Duraisamy, N.; Ponniah, G.; Jo, J.; Choi, K. Structural and Electrical Properties of Ag Grid/Poly(3,4-ethylenedioxythiophene):Poly(styrene Sulfonate) Coatings for Diode Application Through Advanced Printing Technology. *J. Nanosci. Nanotechnol.* **2013**, *13* (8), 5957–5963.

(161) Awais, M. N.; Muhammad, N. M.; Navaneethan, D.; Kim, H. C.; Jo, J.; Choi, K. H. Fabrication of ZrO2 Layer through Electrohydrodynamic Atomization for the Printed Resistive Switch (memristor). *Microelectron. Eng.* **2013**, *103* (2013), 167–172.

(162) Park, J.; Lee, S.; Lee, J.; Yong, K. A Light Incident Angle Switchable ZnO Nanorod Memristor: Reversible Switching Behavior between Two Non-Volatile Memory Devices. *Adv. Mater.* **2013**, *25* (44), 6423–6429.

(163) Choi, K. H.; Ali, A.; Kim, H. C.; Hyun, M. T. Fabrication of Dielectric Poly (4-Vinylphenol) Thin Films by Using the Electrohydrodynamic Atomization Technique. *J. Korean Phys. Soc.* **2013**, *62* (2), 269–274.

(164) Maria, M.; Navaneethan, D.; Chan, K. H.; Taek, H. M.; Hyun, C. K. Solution Processed Fabrication of Single Wall Carbon Nanotubes Thin Film by Electrohydrodynamic Atomization Deposition Technique and Its Characterization. *Appl. Phys. A* **2012**, *109* (3), 515–522.

(165) Hartman, R. P. A.; Brunner, D. J.; Camelot, D. M. A.; Marijnissen, J. C. M.; Scarlett, B. ELECTROHYDRODYNAMIC ATOMIZATION IN THE CONE–JET MODE

PHYSICAL MODELING OF THE LIQUID CONE AND JET. *J. Aerosol Sci.* **1999**, *30* (7), 823–849.

(166) Khan, U.; O'Neill, A.; Lotya, M.; De, S.; Coleman, J. N. High-Concentration Solvent Exfoliation of Graphene. *Small* **2010**, *6* (7), 864–871.

(167) Wu, J.-Y.; Lin, M.-N.; Wang, L.-D.; Zhang, T. Photoluminescence of MoS 2 Prepared by Effective Grinding-Assisted Sonication Exfoliation. *J. Nanomater.* **2014**, *2014* (Cvd), 1–7.

(168) Paton, K. R.; Varrla, E.; Backes, C.; Smith, R. J.; Khan, U.; O'Neill, A.; Boland, C.; Lotya, M.; Istrate, O. M.; King, P.; Higgins, T.; Barwich, S.; May, P.; Puczkarski, P.; Ahmed, I.; Moebius, M.; Pettersson, H.; Long, E.; Coelho, J.; O'Brien, S. E.; McGuire, E. K.; Sanchez, B. M.; Duesberg, G. S.; McEvoy, N.; Pennycook, T. J.; Downing, C.; Crossley, A.; Nicolosi, V.; Coleman, J. N. Scalable Production of Large Quantities of Defect-Free Few-Layer Graphene by Shear Exfoliation in Liquids. *Nat. Mater.* **2014**, *13* (6), 624–630.

(169) Kou, L.; Li, F.; Chen, W.; Guo, T. Synthesis of Blue Light-Emitting Graphene Quantum Dots and Their Application in Flexible Nonvolatile Memory. *Org. Electron. physics, Mater. Appl.* **2013**, *14* (6), 1447–1451.

(170) Skaltsas, T.; Karousis, N.; Yan, H.-J.; Wang, C.-R.; Pispas, S.; Tagmatarchis, N. Graphene Exfoliation in Organic Solvents and Switching Solubility in Aqueous Media with the Aid of Amphiphilic Block Copolymers. *J. Mater. Chem.* **2012**, *22* (40), 21507.

(171) Jan, R.; May, P.; Bell, A. P.; Habib, A.; Khan, U.; Coleman, J. N. Enhancing the Mechanical Properties of BN Nanosheet-Polymer Composites by Uniaxial Drawing. *Nanoscale* **2014**, *6* (9), 4889–4895.

(172) Stankovich, S.; Dikin, D. A.; Dommett, G. H. B.; Kohlhaas, K. M.; Zimney, E. J.; Stach, E. A.; Piner, R. D.; Nguyen, S. T.; Ruoff, R. S. Graphene-Based Composite Materials. *Nature* **2006**, *442* (7100), 282–286.

(173) Kumar, S.; Rezvani, E.; Nicolosi, V.; Duesberg, G. S. Graphene Resist Interlacing Process for Versatile Fabrication of Free-Standing Graphene. *Nanotechnology* **2012**, *23* (14), 145302.

(174) Zhu, C.; Yang, S.; Wang, G.; Mo, R.; He, P.; Sun, J.; Di, Z.; Yuan, N.; Ding, J.; Ding, G.; Xie, X. Negative Induction Effect of Graphite N on Graphene Quantum Dots: Tunable Band Gap Photoluminescence. *J. Mater. Chem. C* **2015**, *3* (34), 8810–8816.

(175) Lin, L.; Zhang, S. Creating High Yield Water Soluble Luminescent Graphene Quantum Dots via Exfoliating and Disintegrating Carbon Nanotubes and Graphite Flakes. *Chem. Commun.* **2012**, *48* (82), 10177–10179.

(176) Beams, R.; Gustavo Cançado, L.; Novotny, L. Raman Characterization of Defects and Dopants in Graphene. *J. Phys. Condens. Matter* **2015**, *27* (8), 083002.

(177) Cançado, L. G.; Jorio, a.; Ferreira, E. H. M.; Stavale, F.; Achete, C. a.; Capaz, R. B.; Moutinho, M. V. O.; Lombardo, a.; Kulmala, T. S.; Ferrari, a. C. Quantifying Defects in Graphene via Raman Spectroscopy at Different Excitation Energies. *Nano Lett.* **2011**, *11* (8), 3190–3196.

(178) Kim, S.; Hee Shin, D.; Oh Kim, C.; Seok Kang, S.; Sin Joo, S.; Choi, S.-H. H.; Won Hwang, S.; Sone, C. Size-Dependence of Raman Scattering from Graphene Quantum Dots: Interplay between Shape and Thickness. *Appl. Phys. Lett.* **2013**, *102* (5), 2012–2015.

(179) Su, Y.; Lu, X.; Xie, M.; Geng, H.; Wei, H.; Yang, Z.; Zhang, Y. A One-Pot Synthesis of Reduced Graphene Oxide-Cu_2S Quantum Dot Hybrids for Optoelectronic Devices. *Nanoscale* **2013**, *5*, 8889–8893.

(180) Peng, J.; Gao, W.; Gupta, B. K.; Liu, Z.; Romero-Aburto, R.; Ge, L.; Song, L.; Alemany, L. B.; Zhan, X.; Gao, G.; Vithayathil, S. A.; Kaipparettu, B. A.; Marti, A. a; Hayashi, T.; Zhu, J.; Ajayan, P. M. Graphene Quantum Dots Derived from Carbon Fibers. *Nano Lett.* **2012**, *12* (2), 844–849.

(181) Dong, Y.; Shao, J.; Chen, C.; Li, H.; Wang, R.; Chi, Y.; Lin, X.; Chen, G. Blue Luminescent Graphene Quantum Dots and Graphene Oxide Prepared by Tuning the Carbonization Degree of Citric Acid. *Carbon N. Y.* **2012**, *50* (12), 4738–4743.

(182) Zhang, L.; Zhang, Z.-Y.; Liang, R.-P.; Li, Y.-H.; Qiu, J.-D. Boron-Doped Graphene Quantum Dots for Selective Glucose Sensing Based on the "Abnormal" Aggregation-Induced Photoluminescence Enhancement. *Anal. Chem.* **2014**, *86* (9), 4423–4430.

(183) Ali, A.; Jo, J.; Yang, Y. J.; Choi, K. H. Direct Fabrication of Graphene/zinc Oxide Composite Film and Its Characterizations. *Appl. Phys. A* **2013**, *114* (2), 323–330.

(184) Borgatti, F.; Park, C.; Herpers, A.; Offi, F.; Egoavil, R.; Yamashita, Y.; Yang, A.; Kobata, M.; Kobayashi, K.; Verbeeck, J.; Panaccione, G.; Dittmann, R. Chemical Insight into Electroforming of Resistive Switching Manganite Heterostructures. *Nanoscale* **2013**, *5* (9), 3954–3960.

(185) Naebe, M.; Wang, J.; Amini, A.; Khayyam, H.; Hameed, N.; Li, L. H.; Chen, Y.; Fox, B. Mechanical Property and Structure of Covalent Functionalised Graphene/epoxy Nanocomposites. *Sci. Rep.* **2014**, *4*, 4375.

(186) Awais, M. N.; Choi, K. H. Resistive Switching and Current Conduction Mechanism in Full Organic Resistive Switch with the Sandwiched Structure of poly(3,4-Ethylenedioxythiophene): Poly(styrenesulfonate)/poly(4-vinylphenol)/poly(3,4-Ethylenedioxythiophene): Poly(styrenesulfonate). *Electron. Mater. Lett.* **2014**, *10* (3), 601–606.

(187) Li, F.; Son, D. I.; Seo, S. M.; Cha, H. M.; Kim, H. J.; Kim, B. J.; Jung, J. H.; Kim, T. W. Organic Bistable Devices Based on Core/shell CdSeZnS Nanoparticles Embedded in a Conducting Poly (N -Vinylcarbazole) Polymer Layer. *Appl. Phys. Lett.* **2007**, *91* (12), 1–4.

(188) Younis, A.; Chu, D.; Lin, X.; Yi, J.; Dang, F.; Li, S. High-Performance Nanocomposite Based Memristor with Controlled Quantum Dots as Charge Traps. *ACS Appl. Mater. Interfaces* **2013**, *5* (6), 2249–2254.